Wegener Center
SCIENTIFIC REPORT
104 | 2024

Estimating AMOC's Variability via In-Situ, Synthetic Remote-Sensing and Model Data

Johannes Unegg

July 2024

Climate Change Graz
Field of Excellence
University of Graz

Wegener Center

UNI GRAZ

The Wegener Center for Climate and Global Change is an interdisciplinary, internationally recognized research and graduate education institute of the University of Graz that is pooling the University's expertise in Climate, Environmental and Global Change. It brings together research teams and scientists from fields such as geophysics and climate physics, meteorology, economics, geography, and social sciences. At the same time, close links are maintained and further developed with many national and international cooperation partners. The research interests range from monitoring, analysis, and modeling of climate and environmental change to the investigation of climate change impacts and the analysis of the human dimensions of these changes related to mitigation, adaptation, and loss & damage. More information at **wegcenter.uni-graz.at**.



Alfred Wegener (1880 – 1930), after whom the Wegener Center is named, was founding holder of the University of Graz Geophysics Chair (1924 – 1930). In his work in the fields of geophysics, meteorology, and climatology he was a brilliant scientist and scholar, thinking and acting in an interdisciplinary way, far ahead of his time with this style. The way of his ground-breaking research on continental drift is a shining role model. His sketch on the relations of continents based on traces of an ice age about 300 million years ago (left) as basis for the Wegener Center Logo is thus a continuous encouragement to explore equally innovative ways: paths emerge in that we walk them (motto of the Wegener Center).

This report is the result of a Master thesis work completed in June 2024.

SR 104 | 2024 Estimating AMOC's Variability via In-Situ, Synthetic Remote-Sensing and Model Data
ISBN 978-3-9505053-3-7 July 2024

Suggested citation:
Unegg, Johannes (2024), Estimating AMOC's Variability via In-Situ, Synthetic Remote-Sensing and Model Data, Wegener Center Scientific Report 104-2024, Wegener Center Verlag, University of Graz, Austria, July 2024. ISBN 978-3-9505053-3-7

(c) 2024 Wegener Center Verlag, University of Graz, Austria
The usage of images, tables, or texts of this Scientific Report is permitted for non-commercial purposes if appropriate credit is given.
For any other purposes, please contact: wegcenter@uni-graz.at

Publishing institution:
Wegener Center for Climate and Global Change, University of Graz
Brandhofgasse 5, 8010 Graz, wegcenter.uni-graz.at

Contact: Johannes Unegg
johannes.unegg@uni-graz.at







Master Thesis

Estimating AMOC's Variability via In-Situ, synthetic Remote-Sensing and Model Data

Johannes Unegg

for the acquisition of the degree
Master of Science

Master Physics with the specialization
Atmospheric Physics and Climate

June 2024

Supervisor Univ.-Prof. Dr. Andrea Steiner[1]
Co-Supervisor Dr. techn. Andreas Kvas[1]

[1]Wegener Center for Climate and Global Change, University of Graz

Abstract

In this thesis, I investigate the fundamental principles and driving mechanisms of the Atlantic Meridional Overturning Circulation (AMOC) and explore the potential of a newly geostrophic Meridional Transport (MT) estimation approach in the North Atlantic (NA). This approach is applied to specified oceanic zonal cross-sections and depth layers, using Ocean Bottom Pressure (OBP) data from in-situ, model, and synthetic remote-sensing data. The AMOC accounts for 25 % of the global meridional heat transport, making its overturning system indispensable for maintaining the temperate climate in Europe. The analysis reveals that the AMOC has been weakening. Hence, the necessity for a monitoring system of the AMOC that is both spatially and temporally continuous is crucial and well justified. The validity of geostrophic MT estimation using OBP integration along the longitudinal extent of the oceanic cross-section is given through comparisons with in-situ Rapid Climate Change-Meridional Overturning Circulation and Heatflux Array (RAPID) data at 26 °N. Further verification is achieved through Ocean Velocity (OVEL) model data from the Estimating the Circulation and Climate of the Ocean (ECCO) model and synthetic remote-sensing data from Gravity Recovery and Climate Experiment/Gravity Recovery and Climate Experiment Follow On (GRACE/GRACE-FO) across the entire NA region. The results imply that MT estimation using solely OBP integration along the longitudinal extent of the cross-sectional ocean bathymetry is feasible, given a bathymetry with a gentle slope and sufficient horizontal extent. The study indicates that the quasi-closed structure of the AMOC causes anomalies in one layer to be mirrored in other layers, suggesting significant interconnectivity among the individual layers. Strong correlations were particularly noted between the Lower North Atlantic Deep Water (LNADW) and Antarctic Bottom Water (ABW). Additionally, variability signals in one specific layer were found to propagate meridionally, with the boundary between the Subtropical and Subpolar Gyres at 40 °N acting as a margin, resulting in different signal characteristics north and south of this region. This study underscored the efficacy of geostrophic MT estimation using solely OBP data for observing AMOC variations, thereby assessing latitudinal coherency and long-term variability. Hence, monitoring the variability of the AMOC offers significant potential for tracking changes in the European climate.

Zusammenfassung

In dieser Arbeit untersuche ich die grundlegenden Prinzipien und Antriebsmechanismen der Atlantisch Meridionalen Umwälzzirkulation (AMU) und das Potenzial eines neuen geostrophischen Ansatzes zur Abschätzung des meridionalen Transports im Nordatlantik (NA). Dieser Ansatz wird auf einen bestimmten ozeanischen zonalen Querschnitt und eine Tiefenschicht angewendet, wobei Ozeanbodendruck (OBD)-Daten aus In-situ-, Modell- und synthetischen Fernerkundungsdaten verwendet werden. Die AMU ist für 25 % des globalen meridionalen Wärmetransportes verantwortlich und somit für das gemäßigte Klima in Europa wichtig. Die Analyse zeigt, dass die AMU eine kontinuierliche Abschwächung erlebt. Daher ist ein räumlich und zeitlich kontinuierliches Monitoringsystem notwendig und gut begründet. Die Gültigkeit der geostrophischen Transportabschätzung durch OBD-Integration entlang des ozeanischen Querschnitts wird durch Vergleiche mit In-situ Rapid Climate Change-Meridional Overturning Circulation and Heatflux Array (RAPID)-Daten bei 26 °N und Vergleichen mit Estimating the Circulation and Climate of the Ocean (ECCO)-Modell- und Gravity Recovery and Climate Experiment/Gravity Recovery and Climate Experiment Follow On (GRACE/GRACE- FO)-Daten über die gesamte NA-Region belegt. Die Ergebnisse zeigen, dass die Schätzung des meridionalen Transports ausschließlich durch OBD-Integration entlang der Querschnittsbathymetrie des Ozeans möglich ist, sofern die Bathymetrie ein gemäßigtes Gefälle und ausreichende horizontale Ausdehnung aufweist. Die Studie zeigt, dass die quasi-geschlossene Struktur der AMU mit Anomalien in einer Schicht, diese in anderen Schichten widerspiegelt, was auf erhebliche Interkonnektivität schließen lässt. Starke Korrelationen wurden besonders zwischen dem Nordatlantischen Tiefenwasser (NAT) und dem Antarktischen Bodenwasser (ABW) festgestellt. Zudem breiten sich Variabilitätssignale meridional aus, wobei die Grenze zwischen subtropischem und subpolarem Wirbel bei 40 °N unterschiedliche Signalcharakteristiken nördlich und südlich dieser Region erzeugt. Diese Studie unterstreicht die Wirksamkeit der geostrophischen Transportabschätzung nur durch OBD-Daten zur Beobachtung von AMU-Variationen und zur Bewertung der meridionalen Kohärenz und langfristigen Variabilität. Daher bietet die Überwachung der AMU-Variabilität erhebliches Potenzial für das Monitoring von Veränderungen im europäischen Klima.

Acknowledgement

Firstly, I would like to express my deepest gratitude to my supervisors, Univ.-Prof. Dr. Andrea Steiner and Dr. techn. Andreas Kvas, for their invaluable guidance and support throughout this journey. Special thanks are due to Dr. techn. Andreas Kvas for his continuous support and input throughout the entire thesis process. His encouragement and the opportunity to work on a topic that I am deeply passionate about, Oceanography, have been instrumental in my academic growth. He provided me the freedom to explore and enhance my analysis independently while offering insightful ideas and guidance on problem-solving. It has been an honor to have his presence and support in this work.

I would also like to extend my thanks to my fellow students for the wonderful times we shared at the university and beyond. Their friendship, partnership, and willingness to lend an ear when needed have been invaluable. In no particular order, thank you to Valerie, Andreas, Diana, Paul, Elvira, Monika, Florian, Samuel, Gabriel, and Martin.

Additionally, I am profoundly grateful to my parents, Silvia and Maximillian, whose support and belief in me have made it possible to study at the University of Graz. Without their encouragement and assistance, none of this would have been possible.

Contents

Abstract i

Acknowledgement v

1 Introduction 1

2 Atlantic Meridional Overturning Circulation 5
- 2.1 What is the AMOC? . . . 5
- 2.2 Drivers of the AMOC . . . 6
- 2.3 Climate Change and AMOC . . . 12

3 Methodology and Data 17
- 3.1 Area of Interest . . . 17
- 3.2 Meridional Transport via Ocean Bottom Pressure . . . 20
- 3.3 Meridional Transport via Ocean Velocity . . . 25
- 3.4 RAPID . . . 26
  - 3.4.1 RAPID Data . . . 29
- 3.5 ECCO . . . 30
  - 3.5.1 ECCO Data . . . 30
- 3.6 GRACE/GRACE-FO . . . 32
  - 3.6.1 Synthetic GRACE/GRACE-FO data . . . 33

4 Results 35
- 4.1 Meridional Transport Estimation from RAPID at 26 °N . . . 35
- 4.2 Validation of Meridional Transport Anomaly Estimation from ECCO . 40
  - 4.2.1 Region of 26 °N . . . 44
  - 4.2.2 North Atlantic . . . 45
- 4.3 Meridional Transport Anomaly Estimation from synthetic GRACE/GRACE-FO . . . 48

5 Discussion 53
- 5.1 Meridional Transport Estimation from RAPID at 26 °N . . . 53
- 5.2 Validation of Meridional Transport Anomaly Estimations from ECCO 55
- 5.3 Meridional Transport Anomaly Estimation from synthetic GRACE/GRACE-FO . . . 58

6 Conclusion and Outlook 61

Bibliography 67

Acronyms

ABW Antarctic Bottom Water. i, 35, 41, 44, 45, 49, 53, 54, 56–59, 61, 62

AMOC Atlantic Meridional Overturning Circulation. i, 1–3, 5–7, 9–16, 20, 24, 26, 28, 29, 32, 33, 35–37, 53–58, 60–63

ARGO Array for Real-time Geostrophic Oceanography. 2

CMIP5 Coupled Model Intercomparison Project 5. 14

CTD Conductivity-Temperature-Depth. 27, 30

DMO Depth of Maximum Overturning. 36, 37, 55

ECCO Estimating the Circulation and Climate of the Ocean. i, 2, 3, 30–34, 40, 44, 45, 48, 49, 55–59, 61, 62

ET Ekman Transport. 7–9, 12, 26, 29, 35, 53, 54

FS Florida Straits. 26, 29, 35, 53, 54, 61

GRACE Gravity Recovery and Climate Experiment. 30–32

GRACE-FO Gravity Recovery and Climate Experiment - Follow On. 32

GRACE/GRACE-FO Gravity Recovery and Climate Experiment/Gravity Recovery and Climate Experiment Follow On. i, 2, 3, 32–34, 48, 49, 58–60, 62

ITCZ Intertropical Convergence Zone. 1, 15

LNADW Lower North Atlantic Deep Water. i, 35, 36, 41, 44, 45, 49, 53, 54, 56–59, 61, 62

MAGIC Masschange and Geosciences International Constellation. 59, 60, 62

MAR Mid Atlantic Ridge. 17, 20, 21, 27, 61

MIES Moored Inverted Echo Sounders. 27

MITgcm Massachusetts Institute of Technology general circulation ocean model. 30

MOC Meridional Overturning Circulation. 29, 35, 36, 53–55, 61

MT Meridional Transport. i, 2, 3, 15, 17, 20–22, 24–26, 28–36, 40, 41, 44, 45, 49, 53–62

NA North Atlantic. i, 1–3, 9–11, 14, 15, 17, 21, 26–29, 33, 36, 40, 45, 49, 53, 55, 57, 58, 61, 62

NH Northern Hemisphere. 1, 5, 6, 8, 10, 15

NOAA National Oceanic and Atmospheric Administration. 26

OBP Ocean Bottom Pressure. i, 2, 3, 17, 20, 23–26, 30–34, 40, 41, 44, 45, 48, 49, 55–62

OHC Ocean Heat Content. 2, 13, 26

OSNAP Overturning in the Subpolar North Atlantic Program. 55, 62

OVEL Ocean Velocity. i, 2, 3, 25, 26, 31, 40, 45, 57, 58, 61

PMOC Pacific Meridional Overturning Circulation. 10

psu Practical Salinity Unit. 9

RAPID Rapid Climate Change-Meridional Overturning Circulation and Heatflux Array. i, 2, 3, 17, 26–29, 32, 33, 35, 36, 40, 44, 55–58, 61

SAMBA South Atlantic Meridional Overturning Circulation Basin-wide Array. 55, 62

SH Southern Hemisphere. 1, 5, 8, 15

SSH Sea Surface Height. 30

SSS Sea Surface Salinity. 9, 10, 30

SST Sea Surface Temperature. 9, 10, 15, 30

UMO Upper-Mid-Ocean. 29

XBT Expandable Bathy-Thermographs. 30

1 Introduction

In recent model studies, the Atlantic Meridional Overturning Circulation (AMOC) has been identified as an essential factor influencing the climate not only in the North Atlantic (NA) and peripheral land masses but globally by means of mass, carbon, and heat transport (Buckley and Marshall, 2016; Smeed et al., 2018; Westen et al., 2024). Differential heating of the Earth and gradients in temperature, salinity, and therefore density, lead to an enormous redistribution of water masses, carbon, and heat. The northward flow of the AMOC is responsible for approximately 25 % of the global meridional heat transport, equating to 1.3 PW, by means of thermal ocean-atmosphere heat exchange over the Atlantic, especially in the NA region (Frajka-Williams, 2015; Bryden et al., 2014). Upper ocean currents, such as the Florida Current and the Gulf Stream transport 30 Sv (Sverdrup) and 15 Sv of water northwards, respectively (1 Sv = 10^6 m^3/s). Northward heat transport is crucial for the European climate. If one compares the latitude of Graz, Austria (46 °N) with a similar latitude on the American Continent, e.g. St.Pierre, Newfoundland (46 °N), a different climate is noticeable. One reason for that is the northward branch of warm upper-ocean currents heading towards Europe, especially the Gulf Stream, North-Atlantic Current, and Norwegian Current (Bryden et al., 2014; McCarthy et al., 2020).

Recent studies have found that the AMOC has experienced reduced overturning in the last years (Bryden et al., 2014; Westen et al., 2024). Climate change is the main driver of a reduced state of overturning primarily due to freshwater influx from meltoff (McCarthy et al., 2020; Westen et al., 2024). Research from Westen et al. (2024) gives additional concern, as they found the first AMOC collapse ever noticed in a model simulation. Such an event has global impacts on the Earth's climate ranging from a shift in the Intertropical Convergence Zone (ITCZ), an increase of the sea ice cover in the Northern Hemisphere (NH), a decrease of the annual mean temperature in Europe, strengthening of the Hadley Cell in the NH amplifying the Subtropical Jet, while the opposite happens in the Southern Hemisphere (SH) (Westen et al., 2024). Especially European climate is influenced the most. According to Westen et al. (2024), the yearly mean temperatures for several European cities could drop by 5 °C to 15 °C after an AMOC collapse according to their model simulation. Even if those scenarios are quasi-impossible to happen in the 21st century and are even very unlikely in the 22nd century, the slowdown of the AMOC is already observed (Bryden et al., 2014; Frajka-Williams, 2015; Smeed et al., 2018).

The AMOC, acting as a vast heat redistributor, is a primary determinant of the climate change trajectory in the NA region and surrounding land masses, particularly Europe. Its role in redistributing and sequestering carbon and heat anomalies significantly influences ocean-atmosphere interactions, sea level rise, the increase of Ocean Heat Content (OHC), acidification of the Atlantic basin, and much more. Enhanced knowledge of the AMOC's dynamics allows for a better representation of this overturning system in climate models, leading to more precise projections of various climate trajectories and an overall better understanding of the AMOC itself. Monitoring the variability of the AMOC gives us the potential to monitor a driver of changing European climate.

Monitoring the variability of the AMOC via in-situ, remote-sensing, and model data in a comprehensive manner is therefore crucial. Changes in the mean state of overturning result in changes in heat flux and hence, alter the European climate. In this thesis, the AMOC for the full available period of in-situ, synthetic remote-sensing, and model data, is examined via estimating Meridional Transport (MT) derived from Ocean Bottom Pressure (OBP) for predefined depth layer categories. In-situ data, containing to some extent the reference, is provided from the Rapid Climate Change-Meridional Overturning Circulation and Heatflux Array (RAPID). Model data, in particular, the data products OBP and Ocean Velocity (OVEL) are delivered by the Estimating the Circulation and Climate of the Ocean (ECCO) model Version 4 Release 4 (V4R4). Remote-sensing, specifically satellite gravimetry data is generated artificially using synthetic Gravity Recovery and Climate Experiment/Gravity Recovery and Climate Experiment Follow On (GRACE/GRACE-FO) data. Remote-sensing offers global coverage, making remote regions like vast oceans accessible (e.g. Steiner et al. (2009)). It further ensures long-term consistency without any mission-to-mission bias and can deliver real-time data (Landerer et al., 2020). However, remote-sensing measures desired quantities indirectly, such as observing OBP anomalies through gravity variations (Tapley et al., 2004). Depending on the mission, remote-sensing can have high initial acquisition costs, however, once launched, there is no need for further maintenance. In-situ measurements provide direct, precise, and accurate data that can be used to correct and validate models and remote-sensing data and vice versa (Abraham et al., 2013). They also offer the capability of real-time data delivery with high precision and accuracy (Abraham et al., 2013). The main disadvantage of in-situ measurements compared to remote-sensing is their regional or local spatial coverage. Achieving global coverage, as in the Array for Real-time Geostrophic Oceanography (ARGO) project requires high costs and constant maintenance (Abraham et al., 2013). Model data, especially reanalysis data, is a combination of model, in-situ, and remote-sensing data. Models contain inherent imperfections as they exist in a self-consistent framework and are based on our theoretical understanding. Combining all these three techniques provides significant added value, offering an extraordinary opportunity to project changes of

the AMOC into the future.

This investigation addresses two primary hypotheses. The first hypothesis examines whether MT anomaly estimation can be facilitated using an approach of OBP integration along the longitudinal direction instead of the depth direction, as done in previous studies (Bingham and Hughes, 2009; Landerer et al., 2015). The second hypothesis investigates whether the MT of the AMOC exhibits latitudinal variation, which in turn makes a strong case for monitoring with remote sensing techniques due to their global coverage, specifically examining if the transport characteristics change meridionally and if there are interconnections between different layers.

An overview of the AMOC is presented in chapter 2. It includes a description of what the AMOC is, the driving mechanisms behind it, and how climate change is impacting the overturning system in principle. Chapter 3 focuses on the area of interest, covering the mathematical reformulation of MT estimation using OBP, the derivation of MT estimation using OVEL, and a description of the datasets used. Chapter 4 examines and analyzes the RAPID array, the ECCO model, and synthetic GRACE/GRACE-FO data. This assessment includes observing in-situ transport data to understand the mean state of the AMOC. We estimate MT anomalies derived from the ECCO OBP model data and compare these estimates with in-situ MT anomalies provided by RAPID. The goal is to determine if the MT anomalies estimated from ECCO data through OBP integration along the longitudinal extent of the zonal cross-section are consistent with the in-situ MT anomalies observed by RAPID at 26 °N in the NA basin. Additionally, we compare the OBP integration estimation methodology by evaluating MT anomalies calculated using OVEL data from ECCO. This localized comparison of model and in-situ MT anomaly estimation extends to the entire NA region, where MT anomalies estimated from ECCO OBP are evaluated against those estimated from ECCO OVEL. Due to the presence of only one in-situ array traversing the entire region of interest zonally (i.e., RAPID), the evaluation of MT anomalies from OBP is limited to comparisons with OVEL anomalies in the rest of the NA region. In the final part of Chapter 4, synthetic GRACE/GRACE-FO data are generated to create a framework for future real GRACE/GRACE-FO MT anomaly estimation using OBP integration, which is then validated against MT anomaly estimations from ECCO OBP data. Chapter 5 provides an overall discussion, while Chapter 6 offers a conclusion and summary.

2 Atlantic Meridional Overturning Circulation

2.1 What is the AMOC?

The AMOC is a coupled system of interconnected ocean currents consisting of a warm northward flow in the upper ocean and a compensating cold southward flow in the deep ocean (Frajka-Williams, 2015; Smeed et al., 2018). Warm northward currents occur between the surface and about 1000 m depth and some examples are the Florida Current, the Gulf Stream, and the North Atlantic Current (Frajka-Williams, 2015; Buckley and Marshall, 2016). Compensating deep and cold southward currents are located between 3000 m and 5000 m depth and are represented by the North Atlantic Deep Water and the Antarctic Bottom Water (Frajka-Williams, 2015; Moat et al., 2023). Surface buoyancy loss in the high-latitude North Atlantic and wind-driven mixing in the Southern Ocean contribute to water mass conversion (see section 2.2). The AMOC plays an indispensable role in global heat, carbon, and oxygen distribution and is the link between the SH and the NH via water and heat transport (Buckley and Marshall, 2016). Furthermore, it is the main cause of interhemispheric asymmetries in the climate system (Buckley and Marshall, 2016). In the ocean, convection is mainly driven by buoyancy loss at the surface, especially at polar latitudes (Buckley and Marshall, 2016). Therefore, convection cells in the ocean, especially in the Atlantic basin, originate mainly in the polar regions (Buckley and Marshall, 2016). These convection cells are called Meridional Overturning Cells (Buckley and Marshall, 2016). The AMOC is composed of an upper cell that ventilates the upper 2000 m of the ocean column originating in the Arctic, and a lower cell that mixes the deep and abyssal ocean originating in the Antarctic (Buckley and Marshall, 2016). In Figure 2.1 the AMOC's currents are depicted schematically. Red lines indicate northward heading, warm upper-ocean currents like the Florida Current, Gulf Stream, and North Atlantic Current. Blue lines represent southward heading, cold deeper-ocean currents like the North Atlantic Deep Water. Regions, where the initially warm surface waters reach a critical density due to surface buoyancy, loss are entitled as Deep Water Formations. Due to wind-induced Ekman Transport, the Subtropical- and Subpolar Gyres arise. More information in this context see in section 2.2.

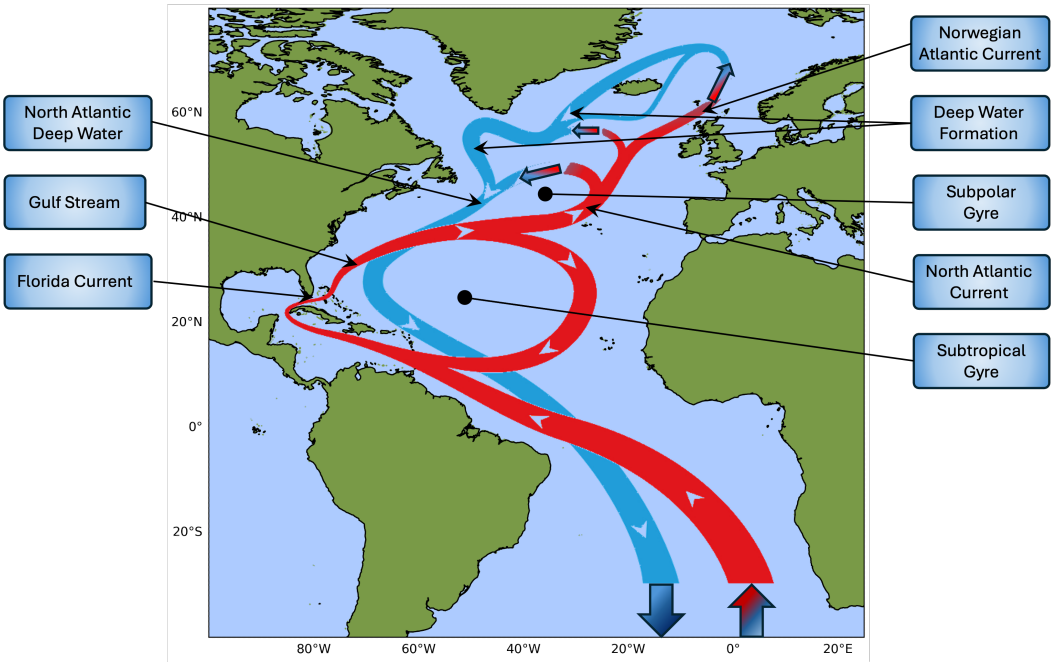


Figure 2.1: Structure of the AMOC in the North Atlantic.

In terms of heat redistribution, the northward-flowing currents of the AMOC play a crucial role for the NH, especially for Europe (Frajka-Williams, 2015). Comparing regions of the same latitude on the North American continent and in Europe reveals that European regions, particularly Western Europe, have a much more temperate climate. For instance, at the latitude of 40 °N, New York is located on the East Coast of North America, while Naples is located at the same latitude in Europe. These two cities experience completely different climates, largely due to the heat transport by the northward currents of the AMOC, in particularly the North Atlantic Current (Frajka-Williams, 2015; Bryden et al., 2014). According to recent studies, the northward branches of the AMOC are responsible for about 25 % of the global meridional heat transport, equating to around 1.3 PW (Frajka-Williams, 2015; Bryden et al., 2014). Bryden et al. (2014) demonstrate that the overturning mechanism of the AMOC is undergoing a reduction (Bryden et al., 2014). Since 1950 the AMOC has weakened by 3 ± 1 Sv (Caesar et al., 2018). During 2009 and 2010 an abrupt weakening of the mean state of about 30 % was recorded and these events coincided with cold winters in Europe (Bryden et al., 2014).

2.2 Drivers of the AMOC

The AMOC system has two main drivers, wind forcing and gradients in density (Buckley and Marshall, 2016). Water transport due to zonal wind forcing on the surface of the ocean is mainly responsible for the transport in the upper layers of the ocean (Buckley and Marshall, 2016). Transport due to wind forcing takes place in

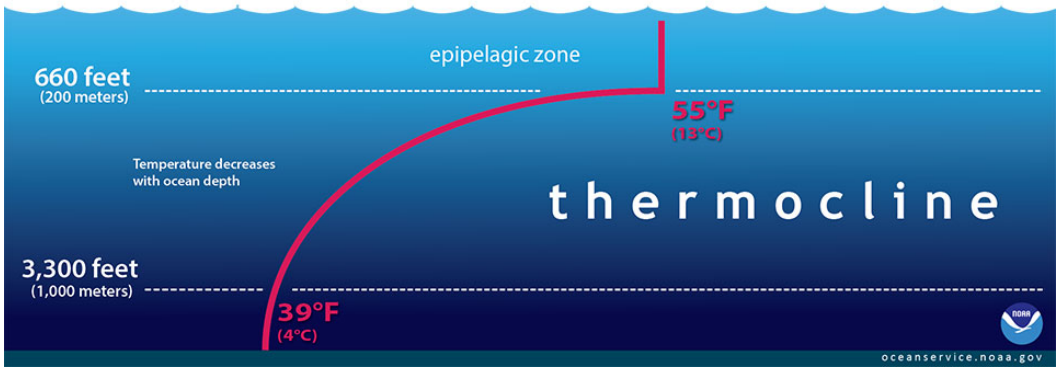


Figure 2.2: Structure of the Thermocline (NOAA, 2024).

the epipelagic zone or so-called mixed layer between the surface and approximately 200 m in depth, seen in Figure 2.2. Mixed layer depth depends on the latitude and season, ranging from 40 m to 300 m (Stewart, 2006). Concerning intra-annual timescales, the variability of the AMOC is large and mainly reflects the feedback to local wind forcing (Buckley and Marshall, 2016). Variability can be calculated from the zonal wind stress τ_λ and its seasonal cycle ranges from -1 Sv to 2 Sv (Ivchenko et al., 2011). The underlying principle behind water transport due to

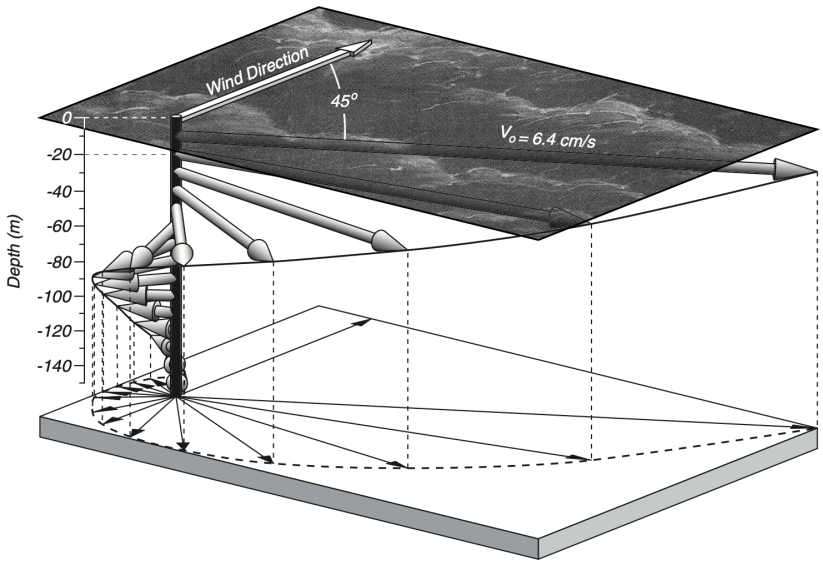


Figure 2.3: Schematic demonstration of the Ekman Spiral (Stewart, 2006); licensed by CC BY-NC-ND 3.0.

wind forcing is the so-called Ekman Transport (ET). The first contributor to the theory of wind-driven circulation was Fridtjof Nansen, a Norwegian oceanographer, who noticed that icebergs drift perpendicular to the surface wind direction (Stewart, 2006). Endpoints of the velocity vectors in Figure 2.3 describe in a geometrical sense a Hodograph, i.e. the Ekman-Spiral. The Ekman Spiral is an explicit stationary solution of the Navier-Stokes Equations, resulting from a combination of the Coriolis-

($\vec{F}_c$) and frictional force ($\vec{F}_r$)(Stewart, 2006), i.e. the drag. At the surface, according to the direction of the wind, the water is deviated by 45 ° to the right on the NH and to the left on the SH. Due to friction, the layer beneath also moves but with a smaller velocity and is additionally further deflected by $\vec{F}_c$. The strength of ET, i.e. velocity, decreases exponentially with depth as the friction increases until the Ekman layer depth D_e is reached. At D_e, a weak countercurrent, opposing the direction of the surface flux, appears (Stewart, 2006). Integrating the velocity vectors along depth gives the resulting total flow, which has a net transport direction of 90 ° in comparison to the surface winds (Stewart, 2006). On the NH, net water transport is 90 ° to the right in the sense of the surface winds, and vice versa for the SH. Coastal upwelling and downwelling, i.e. Ekman pumping (vertical flow in the ocean) are features of the oceans due to ET (Stewart, 2006). Tradewinds from the north-

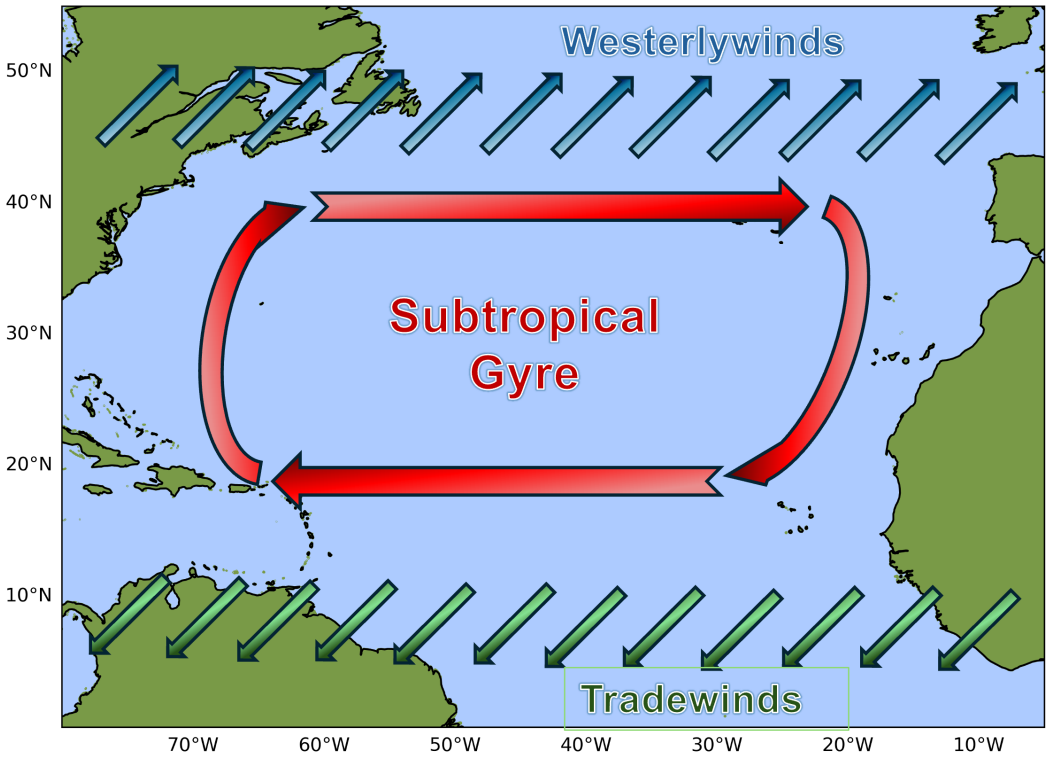


Figure 2.4: Pattern of the wind-induced Subtropical Gyre in the North Atlantic.

east at lower latitudes and Westerlies from the south-west at mid-latitudes cause convergent ET which in turn forces the water masses to pile up at around 30 °N (seen in Figure 2.4) forming the Subtropical Gyre (Stewart, 2006). The center of the vortex is shifted to the west, since the ET has a westerly component through the Tradewinds, leading to an intensification of the western boundary currents and an attenuation of the eastern boundary currents (Stewart, 2006). According to Sverdrup, the absolute vorticity in a closed gyre has to be conserved and friction and shear at the western boundary provide a positive vorticity (Stewart, 2006). The westerly component of Subtropical Gyres and the theorem of Sveredrup are the main

reasons for strong and narrow western boundary currents as for example the Gulf Stream or Kuroshio and smooth and wide eastern boundary currents as the Canary Current or the California Current. Ocean gyres especially the Subtropical ones, are the most important feature emanating due to ET. They dictate the main propagation patterns of water masses in the world's oceans. In terms of the North Atlantic, the Subtropical Gyre is centered at the Horse Latitudes (around 30 °N), and the Subpolar Gyre is centered at approximately 60 °N seen in Figure 2.1. An important region is found in a western "transition zone" beside the boundary between the Subtropical and Subpolar Gyre. This region is a pacemaker in the sense of decadal AMOC variability and these decadal changes are transmitted meridionally from this boundary region (Buckley and Marshall, 2016). According to Bingham and Hughes (2009), low-frequency modes (i.e. decadal variability) are apparent in this transition zone (46 °N) in comparison to further south, as the weak stratification of the NA Subpolar Gyre does not allow for waves to travel as freely as in the Subtropical Gyre. Hence, this transition zone between the Subtropical and the Subpolar Gyre could be used to obtain a clearer picture of decadal AMOC variability as it could be retrieved from further south.

The second main driver of the AMOC are gradients in density (Buckley and Marshall, 2016). AMOC strength goes hand in hand with large-scale meridional density gradients, as stronger gradients imply a stronger circulation (Buckley and Marshall, 2016). The interplay of temperature differences and salinity means that seawater has different buoyancy properties depending on the season, latitude, and depth (Buckley and Marshall, 2016). Differential heating of the Earth's surface leads to temperature gradients between the Equator and the poles. The equator receives more direct sunlight than the poles. This creates temperature gradients across the globe. In Figure 2.5 the global Sea Surface Temperature (SST) for 2017 is depicted. Equatorial regions show a much higher SST as in comparison to higher latitudes. According to the 2nd law of thermodynamics, heat can only be transferred from warm to cold and not the other way around (Demtröder, 2021). The differential heating of the Earth's surface leads to an imbalance in the distribution of heat in the system, in terms of the oceans seen in Figure 2.5. The climate system responds to these imbalances by moving heat from warmer to cooler areas. In terms of the ocean, the redistribution of heat is carried out by ocean currents and evaporation.
A further major factor influencing the density of seawater is salinity. It is an important property in terms of buoyancy. Salinity depends mainly on the evaporation and precipitation rates, freshwater influx and on the sea ice formation rate (Stewart, 2006). The global Sea Surface Salinity (SSS) for 2017 is shown in Figure 2.6. SSS is given in Practical Salinity Unit (psu) which corresponds to g of salt per kg of seawater. Concerning the Atlantic, two regions of high SSS are visible at around 30 °N/S, indicated by light yellow areas. These regions are the so called Horse Latitudes, where evaporation is stronger than precipitation. An indicator for AMOC stability

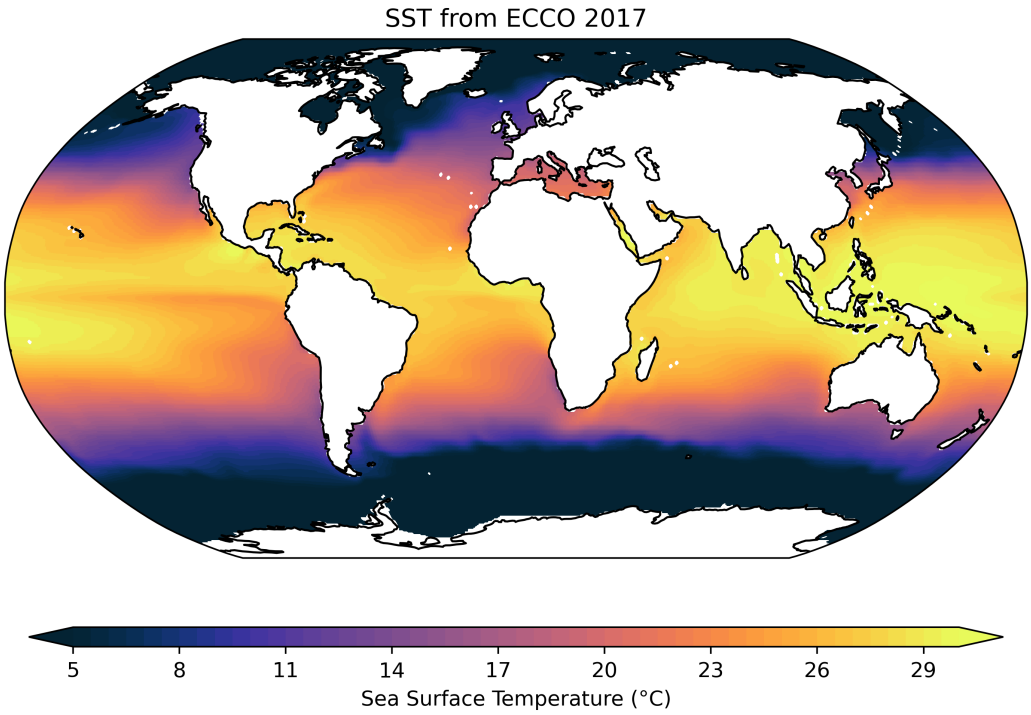


Figure 2.5: Global Sea Surface Temperature from ECCO for 2017.

often discussed in the literature, is the so-called Salt-Advection Feedback (Buckley and Marshall, 2016; Westen et al., 2024). In terms of buoyancy, salinity plays a superior role in the relatively cold Subpolar Gyre than in the warm Subtropical Gyre (Buckley and Marshall, 2016). At higher latitudes, ice formation and the associated bryne rejection increase salinity, whereas the melting of ice leads to a decrease of salinity. Intraannual SST anomalies tend to be damped due to the high specific heat capacity of the oceans, whereas the freshwater fluxes are not (Buckley and Marshall, 2016). As an outcome, high-frequency SST anomalies will experience stronger attenuation than SSS. This indicates, that in terms of buoyancy, the salinity especially the SSS has a bigger impact than the SST (Buckley and Marshall, 2016).

The overturning pattern of the AMOC is unique and not found in other ocean basins, i.e. there is, for example, no Pacific Meridional Overturning Circulation (PMOC). One major contributing factor is the glaciation of the NH. It started around 2.4 Ma ago when the climate changed from a warm Pliocene to the NH ice ages in the Pleistocene epoch (Raymo, 1994). As the NH got cooled by the glaciation, the oceans did as well in that region, leading to higher densities at polar latitudes. In addition to having higher salinity, the NA is also more connected to the Arctic than the North Pacific is (Johnson et al., 2019). Cessi and Jones (2017) show that in a numerical model of the oceans state in two idealized ocean basins, representing the Pacific and the Atlantic separated by two narrow continents and interconnected by a circumpolar passage to the south, the SSS in the narrower basin (Atlantic) is nearly

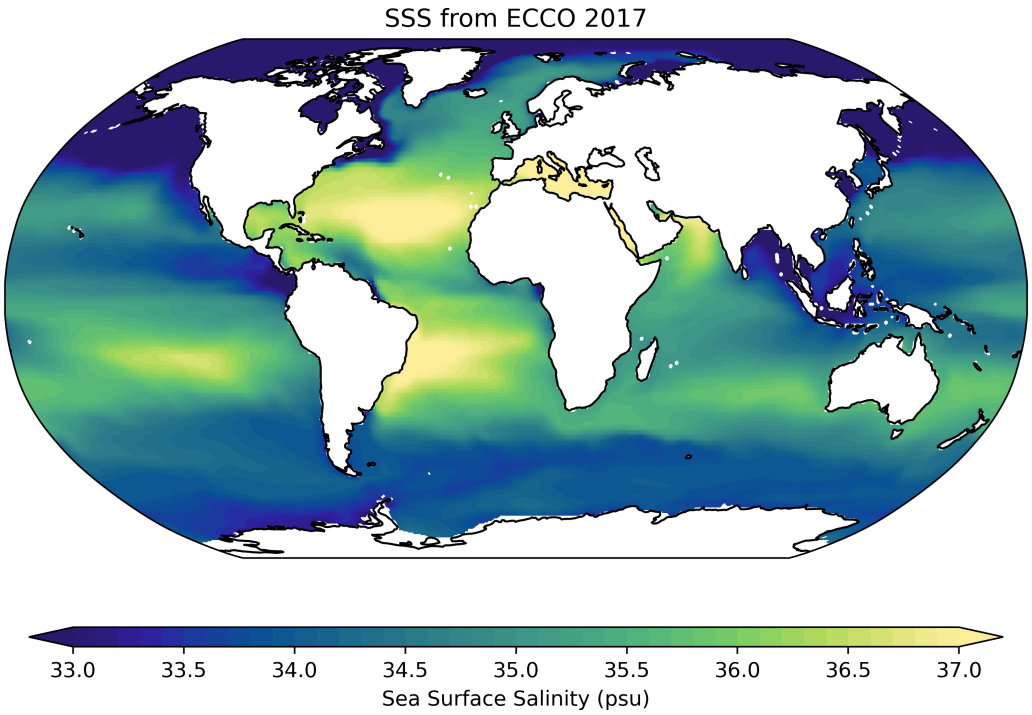


Figure 2.6: Global Sea Surface Salinity from ECCO for 2017.

2 psu higher than in the wide basin (Pacific) (seen in Figure 2.7). Furthermore, the subtropical interbasin conjunction at 35 °S is indispensable for the salinization of the narrower basin, which corresponds to salt advection from the Indian Ocean (Cessi and Jones, 2017; Johnson et al., 2019). The model of Cessi and Jones (2017) demonstrates that a salinity increase of $\Delta S = +2$ psu in the narrow basin, can lead to deep water formations in the polar regions and vice versa, a decrease of $\Delta S = -2$ psu can lead to the vanishing of them. An increase in AMOC strength, leads to enhanced salt and heat advection into the high-latitude sinking region (Johnson et al., 2019). Due to the atmospheric-oceanic interplay, evaporation cools the surface currents further as they travel towards higher latitudes, e.g. North-Atlantic and Norwegian Current (Buckley and Marshall, 2016). Positive salt anomalies decrease surface buoyancy, creating positive feedback (salinity-advection feedback), whereas positive temperature anomalies increase buoyancy and provide negative feedback on AMOC strength (temperature-advection feedback) and vice versa (Johnson et al., 2019). Surface waters will cascade down when the density of the water reaches a critical level, forming the so-called deep water formations. According to Bingham and Hughes (2009), the rate of deep water formation is linked to the North Atlantic Oscillation (NAO). To summarize, enhanced cooling due to the more connected NA basin to the Arctic, stronger salt advection from other basins, and higher salinity of the Atlantic in general compared to the Pacific is key to deep water formation in polar regions and indispensable for the development of an AMOC (Buckley and Marshall, 2016; Johnson et al., 2019; Westen et al., 2024).

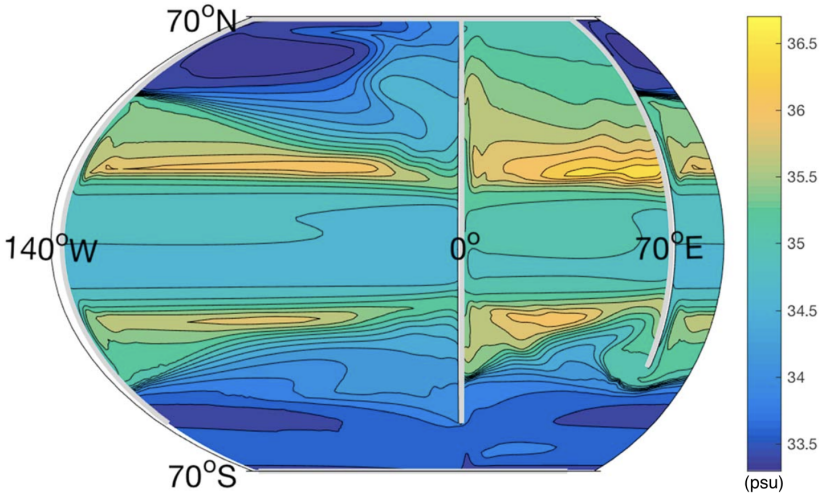


Figure 2.7: Time-mean surface salinity in a numerical model from Cessi and Jones (2017) of the ocean circulation in two idealized basins separated by narrow continents represented by gray zonal lines (Johnson et al., 2019); licensed by CC BY 4.0.

A fundamental question that remains is whether AMOC variability can be understood concerning a single variable (buoyancy) or whether a three-component equation of state (wind, temperature, and salinity) needs to be considered. The time scale is the main factor influencing AMOC variability. On shorter time scales, winds, i.e. ET dominate, whereas on decadal time scale, the AMOC seems to be controlled by buoyancy anomalies (Buckley and Marshall, 2016). Due to the weaker damping, salinity anomalies on longer time scales are likely to play a more significant role in the variability of the AMOC compared to temperature anomalies, which are dampened by the ocean's thermal inertia (Buckley and Marshall, 2016).

2.3 Climate Change and AMOC

Anthropogenic climate change is causing disequilibrium in the Earth's energy budget, leading to excessive heat within the climate system and an energy imbalance at the top of the atmosphere (Meyssignac et al., 2019; Von Schuckmann et al., 2023). The oceans act as the main storage for anthropogenic produced heat and carbon in the climate system (Zanna et al., 2019; Arrigo et al., 2008). Estimates show that through physical and biological processes, 25 % to 35 % of CO_2 is sequestered into the ocean interior (Arrigo et al., 2008). Due to the high specific heat capacity of water ($c_{p,\mathrm{H_2O}} \approx 4190 \frac{J}{kgK}$ (Verein Deutscher Ingenieure et al., 2002)), the oceans have enormously high thermal inertia and therefore act as a main sink of heat in the climate system. Several studies show that the oceans have been absorbing over 93 % of anthropogenically produced heat since 1955 (Abraham et al., 2013; Meyssignac et al., 2019). Zanna et al. (2019) demonstrate that these 93 % amount

up to 436 ± 91 ZJ (!) of energy stored in the oceans interior. Sequestration of these heat and carbon anomalies is one of the key mechanisms of the AMOC and is only possible because of the underlying convective processes emanating from the Atlantic Basin (Johnson et al., 2019). The AMOC is therefore crucial in integrating excess heat and carbon into the ocean interior, thereby modulating the trajectory of climate change. (Buckley and Marshall, 2016).

Although the oceans appear to have an infinite capacity to store heat and carbon, there is a finite capability to sequester these anomalies into the interior. The main impacts of buffering these anomalies are perceivable in the increase of the OHC and the acidification of the oceans (Meyssignac et al., 2019; Cheng et al., 2024; Garcia-Soto et al., 2021). Especially the increase of OHC is impacting AMOC strength. In the period from 1950 to 2019 the OHC increased by $0.35 \pm 0.08\,\mathrm{W/m^2}$ (Garcia-Soto et al., 2021). The increase doubled for the last full decade (2010 to 2019) up to $0.70 \pm 0.07\,\mathrm{W/m^2}$, which led to the warmest 10 years by means of OHC since records have been kept (Garcia-Soto et al., 2021). The remaining 7 % of the excessive heat produced by human activity flows into the warming of the atmosphere and the continents, as well as the melting of sea and land ice. (Wouters, Wal, et al., 2018; Von Schuckmann et al., 2023). In particular the melting of ice sheets, primarily the influx from the Greenlandic Ice Sheet affects the strength and stability of the AMOC (Westen et al., 2024). The freshwater influx from the Greenlandic Ice Sheet influences buoyancy in the regions of deep water formation. Meltwater has a lower density than seawater due to virtually no salt contained within. This results in increased surface buoyancy and reduced sinking capability in regions of deep water formation (Buckley and Marshall, 2016). Consequently, there is a weakening of the overturning circulation resulting from an increase of surface buoyancy due to freshwater influx from meltwater, which is reflected in the diminished strength of the AMOC (Westen et al., 2024).

The AMOC is influenced by three key drivers, as discussed in section 2.2. Climate change impacts these drivers through the accumulation of excess heat in the oceans, changes in wind patterns, and the influx of freshwater from ice sheets, ice caps, and glaciers, all of which disrupt the overturning processes (Buckley and Marshall, 2016; Westen et al., 2024). These factors lead to alterations in the dynamics of overturning due to:

- Changes in the wind system $\rightarrow$ Ekman Transport and zonal wind shear (τ_λ)
- Increase in Ocean Heat Content $\rightarrow$ Smaller meridional temperature gradients (∇T)
- Meltwater influx $\rightarrow$ Increase in buoyancy due to changes in salinity (∇S)

Recent research indicates that the AMOC is undergoing a phase of diminished overturning (Bryden et al., 2014; Smeed et al., 2018; Caesar et al., 2018). Additionally, proxy records have suggested that the AMOC is in its weakest state in over 1000 years (Westen et al., 2024).

An additional concern arises due to the study and model simulation from Westen et al. (2024). The study uses the Community Earth System Model (CESM) by running a targeted simulation to estimate the AMOC with steadily increasing meltwater influx to derive an early warning indicator for AMOC tipping. Westen et al. (2024) start with a statistical equilibrium solution, which means that the model simulation is realized with constant held greenhouse gas concentration, solar and aerosol forcing, corresponding to preindustrial levels. A slowly increasing freshwater anomaly is added in the NA between 20 °N and 50 °N (Westen et al., 2024). The freshwater influx increases by 3×10^{-4} Sv/a until model year 2200 (Westen et al., 2024). This kind of simulation has not been previously conducted with a complex Global Climate Model (GCM) like those employed in Coupled Model Intercomparison Project 5 (CMIP5).

As seen in Figure 2.8 (A) the strength of overturning, i.e. maximum of the stream

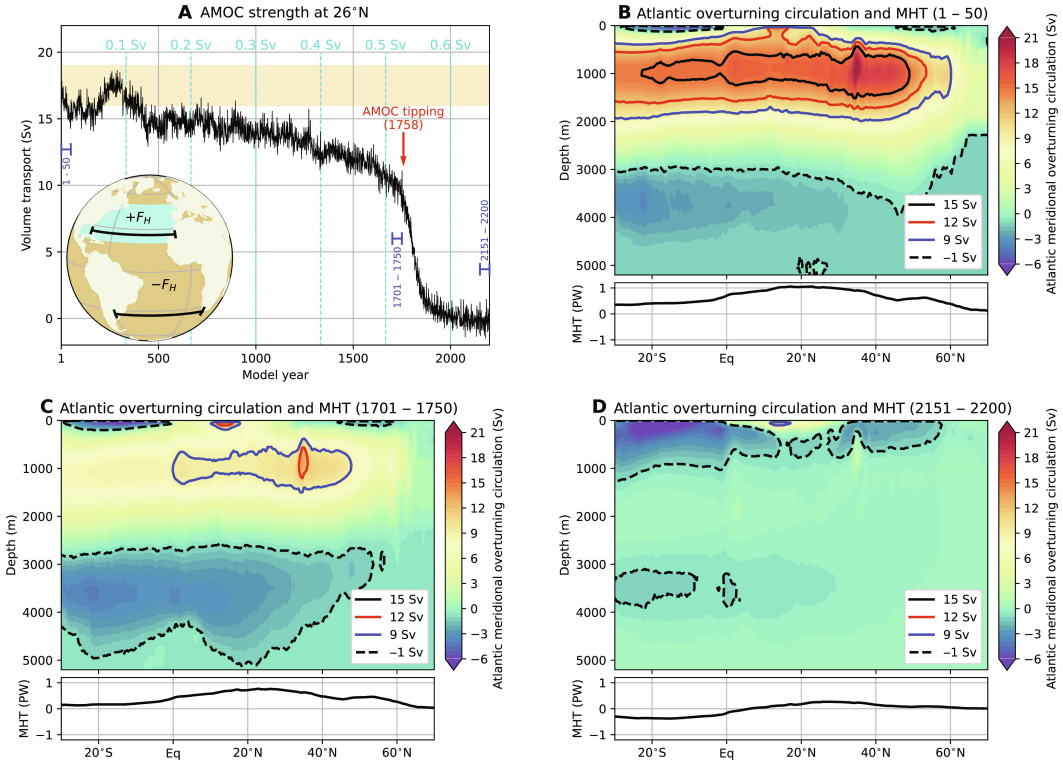


Figure 2.8: (A) AMOCs strength at 26 °N and 1000 m depth. (B)(C)(D) Streamfunction ζ_ϕ and Meridional Heat Transport (MHT) for different model periods (Westen et al., 2024); licensed by CC BY 4.0.

function (see Equation 3.20), gradually decreases. After 400 model years, internal variability still dominates AMOC strength. A negative trend appears around

800 years of simulation. In the model year 1758, an abrupt tipping of the AMOC strength occurs, leading to a total collapse (Westen et al., 2024). Yellow shading indicates observed ranges of AMOC variability (Westen et al., 2024). In Figure 2.8 (B), (C), and (D) the stream function ζ and the Meridional Heat Transport (MHT) are depicted. The stream function ζ is the cumulative integral of MT over depth (see Equation 3.20) and is estimated in the model simulation for 26 °N and 34 °S cross sections indicated by black-latitudinal lines in Figure 2.8 (A) (McCarthy et al., 2015; Westen et al., 2024). AMOC strength is defined as the maximum of ζ at a certain latitude (for further information see section 3.2). The region of gradually increasing freshwater influx is indicated as a light blue area between 20 °N and 50 °N ($+F_h$) and is also apparent as values in light blue in (A). $-F_h$ stands for the compensation of the freshwater influx by the remaining ocean surface.

Westen et al. (2024) suggest the freshwater transport (F_{ovs}) of the AMOC at 34 °S as physics-based early warning indicator for AMOC tipping. F_{ovs} is a strong indicator for the salt-advection feedback (see section 2.2), which is crucial for the deep water formation at polar latitudes. Additionally, F_{ovs} signifies the amplification of a freshwater input perturbation by a weakening of the overturning, resulting in reduced northward salt advection (Westen et al., 2024). Prior to the collapse of the AMOC, salinity changes at 34 °S exceed changes in meridional velocity, suggesting that variations in F_{ovs} are mainly attributed to changes in salinity (Westen et al., 2024). 25 days in advance of the collapse, F_{ovs} goes through a minimum (Westen et al., 2024). Westen et al. (2024) demonstrate that F_{ovs}, especially it's minimum along with an increase in variance, serves as a highly promising physics-based early warning indicator for a future impending AMOC collapse. The collapse of the AMOC leads to significant changes in SST, affecting the NH and SH differently and influencing global climate patterns, including shifts in the ITCZ and changes in sea ice distribution (Westen et al., 2024). The concern is given as results from Westen et al. (2024) indicate a cooling of the SST near Western Europe by 10 °C and dynamic sea level rise in the Atlantic basin by magnitudes of 70 cm according to geostrophy after the AMOC collapses.

Paleo climatological proxy data support the occurrence of rapid AMOC changes, especially during Dansgaard-Oeschger events, as outlined by Renssen et al. (2015) and Westen et al. (2024). Proxy data indicate that the most recent collapse of the AMOC occurred during the Younger Dryas period (around 11.6 ka) (Renssen et al., 2015). The prevailing theory posits that this significant climatic event was triggered by the drainage of Lake Agassiz, which resulted in a substantial freshwater influx into the NA, disrupting the overturning circulation (Renssen et al., 2015). However, it is important to consider that the study by Westen et al. (2024) represents just a single model run, constrained by high computational and financial costs. Additionally, throughout the simulation period, radiative forcings such as

greenhouse gases, aerosols, and other factors were maintained at constant levels. Regarding present conditions, the study indicates that for an AMOC collapse to occur, the freshwater influx from melting would need to increase by 80 times in comparison to the current rate, reaching an astonishing flux of 0.65 Sv, equivalent to 650.000 m^3/s (Westen et al., 2024). Consequently, a shut-down of the AMOC in the 21st century appears highly improbable. Despite these limitations, the integration of model studies together with historical data on AMOC slowdowns or collapses, such as the Younger Dryas event documented in proxy data (Renssen et al., 2015), provides crucial insights. This combination will be invaluable for projecting and detecting a potential future collapse of the AMOC.

3 Methodology and Data

3.1 Area of Interest

In this work, we focus on the NA region spanning from 10.0 °N to 66.5 °N and from 10.0 °W to 80.0 °W. There are several reasons for selecting this specific area. Firstly, the RAPID array is situated within this region, traversing meridionally through 26 °N, providing a valuable opportunity to compare the estimated MT anomaly from OBP data (see Equation 3.19). The MT estimation by Equation 3.19 is based on geostrophy, meaning that we have to exclude the equatorial region due to the vanishing Coriolis force. Additionally, the deep water formations occurring at higher latitudes are apparent, as shown in Figure 2.1. Furthermore, this region encompasses major ocean currents, including the warm, upper ocean northward currents such as the Gulf Stream and North Atlantic Current, and cold southward currents like the Deep Western Boundary Current, as illustrated in Figure 2.1. The red rectangle in Figure 3.1 highlights the research area corresponding to the NA. In this region, the Mid Atlantic Ridge (MAR) is clearly visible, dividing the Atlantic into a western and an eastern basin, traversing the entire Atlantic in a quasi-meridional direction. Figure 3.2 shows a zoomed-in view of the red rectangle from Figure 3.1. This region is the primary focus of our research, and all further investigations were conducted within these boundaries. To gain a better understanding of the bathymetry structure, a 3D plot is provided in Figure 3.3. High-elevated areas correspond to the continental shelves and the continents themselves. In Figure 3.3, the east coast of the North American continent is schematically visible on the left side, while the west coasts of Africa and Europe are schematically shown on the right side. The MAR is also visible as it traverses the entire NA basin meridionally, dividing the Atlantic into a western and an eastern basin.

The 3D plot in Figure 3.3 is essential for understanding the steepness of the continental shelf flanks toward the Atlantic Basin. This steepness is crucial as it influences the distribution of OBP values on the bathymetry slope. Previous studies (Bingham and Hughes, 2009; Landerer et al., 2015; Frajka-Williams, 2015) relied on distinguishing between the western and eastern flanks, which is not straightforward due to the intervening topography of the MAR. The MAR, with its western and eastern flank as intervening bathymetry, demonstrates the necessity for a reformulation of the MT estimation from geostrophy as conducted by previous studies.

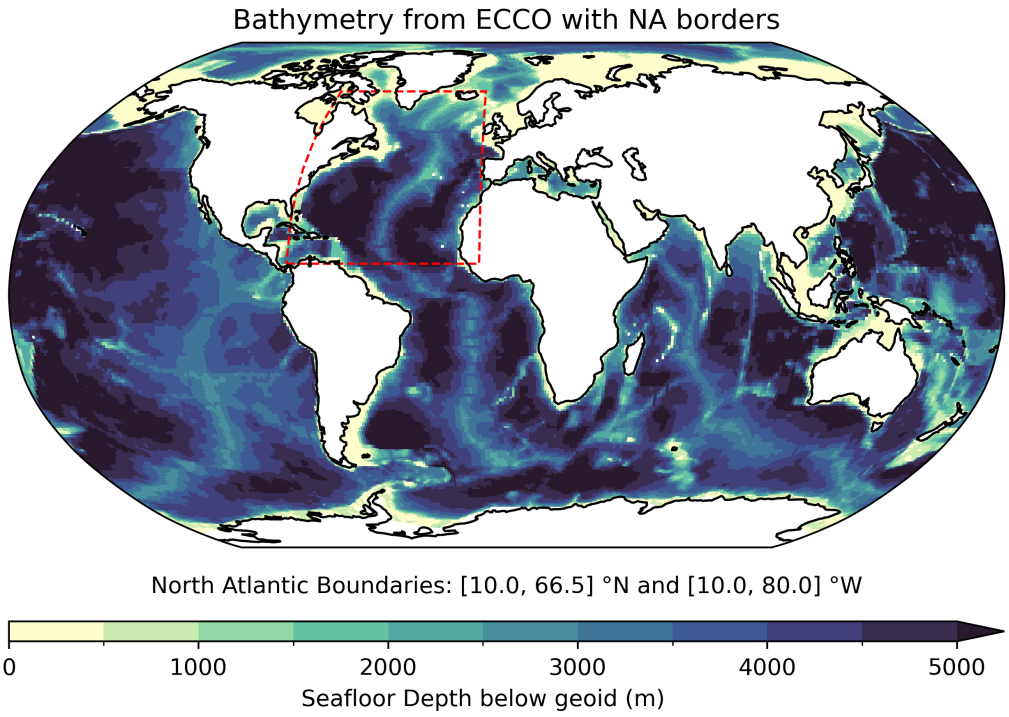


Figure 3.1: Bathymetry of the global oceans from ECCO model data and boundary of the research area, i.e. North Atlantic, indicated by a red rectangle.

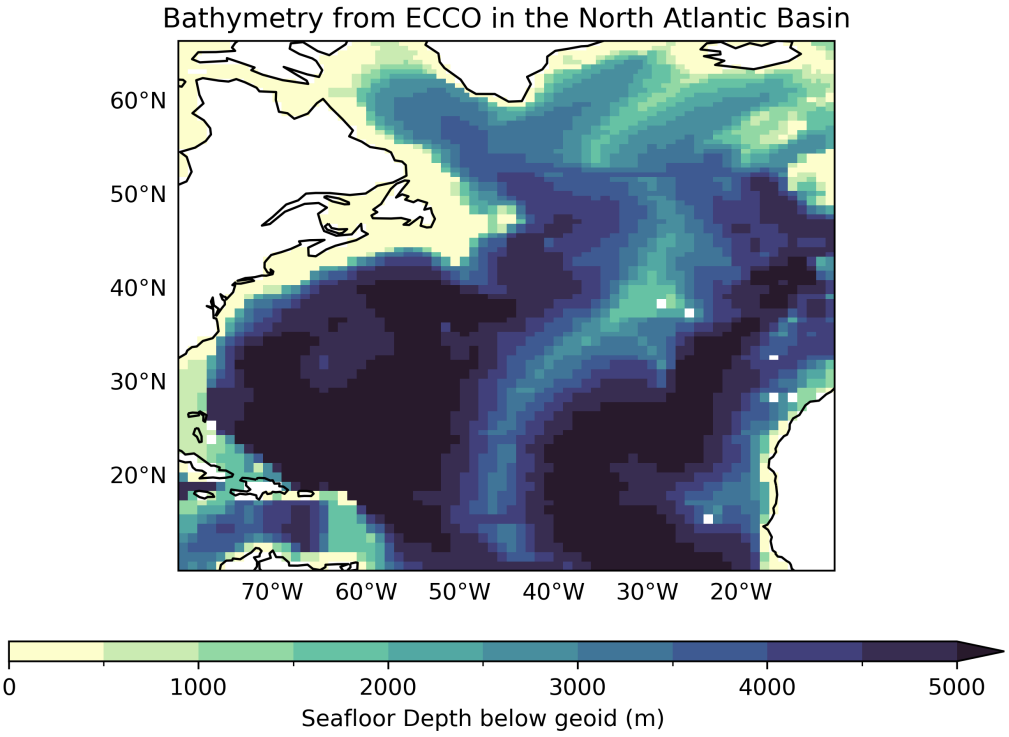


Figure 3.2: Bathymetry of the North Atlantic basin with corresponding Seafloor Depth below geoid from ECCO data.

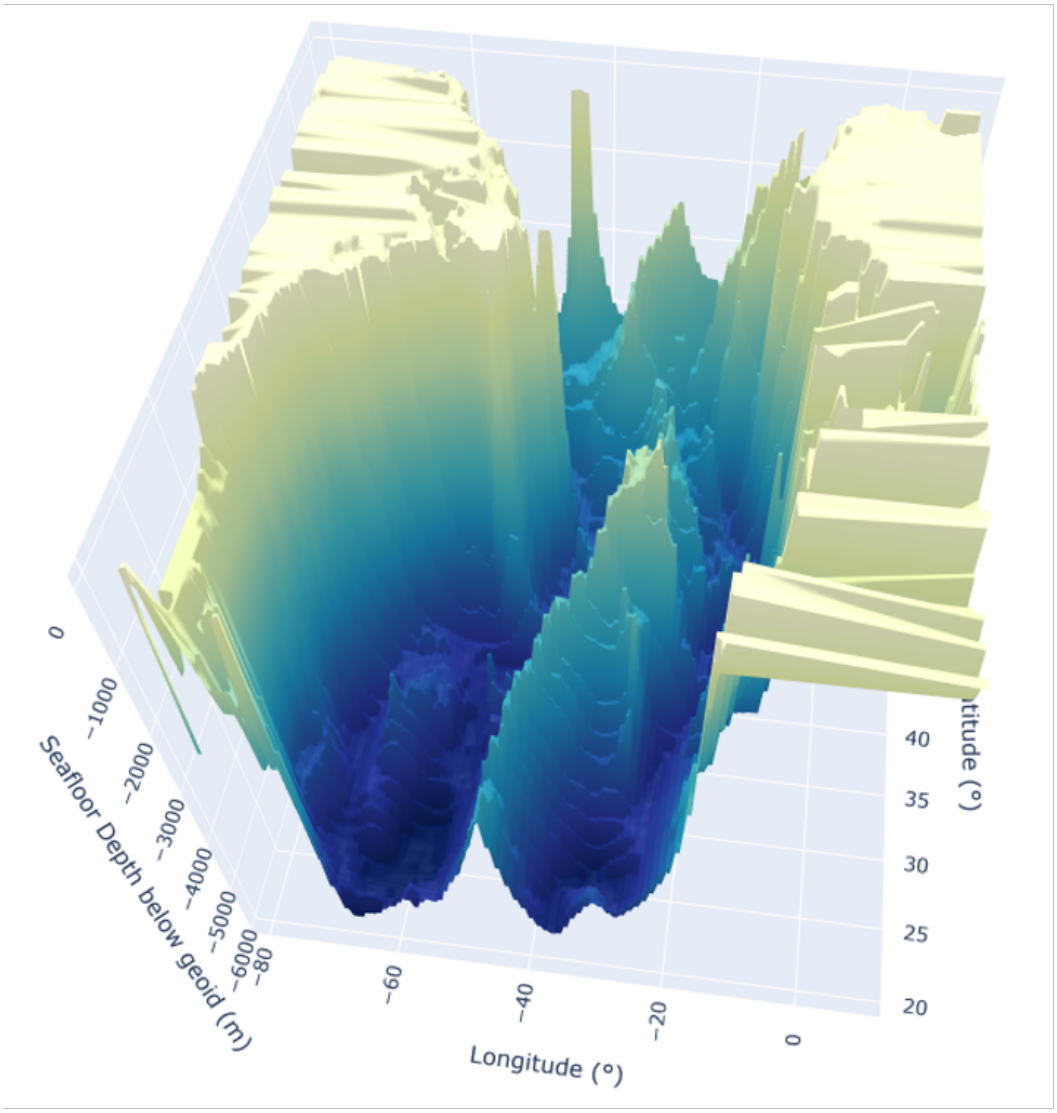


Figure 3.3: Bathymetry of the North Atlantic basin in 3D from ECCO data.

3.2 Meridional Transport via Ocean Bottom Pressure

In the context of AMOC monitoring, we are interested in the so-called MT. It is the flux of ocean water through a cross-section of constant latitude, i.e. a zonal cross-section. Following the concept of geostrophy without intervening bathymetry, the MT according to Bingham and Hughes (2009) reads,

$$\Psi_\phi(z) = \frac{1}{\rho_0 \, f_\phi} \int_{z_{\text{min}}}^{z_{\text{max}}} (p_e^b(z) - p_w^b(z)) \, dz \tag{3.1}$$

which gives the MT for a certain latitude and depth layer between z_{min} and z_{max}. The integrand is the zonal pressure difference at a certain depth between the OBP on the eastern $p_e^b(z)$ and western $p_w^b(z)$ flank, respectively. The term

$$\rho_0 = 1029 \text{ kg/m}^3 \tag{3.2}$$

corresponds to the average density of seawater, which is assumed to be constant and is certainly justified as horizontal density variations are generally small, especially in deeper layers. The Coriolis parameter for a certain latitude reads,

$$f_\phi = 2 \, \Omega \, \sin(\phi) \tag{3.3}$$

with the angular velocity of the Earth given as,

$$\Omega = 7.2921 \times 10^{-5} \text{ rad/s} \tag{3.4}$$

In many past studies (Kanzow et al., 2009; Bingham and Hughes, 2009; Landerer et al., 2015) Equation 3.1 was used, but the estimation of MT in this manner is very laborious, as we have to define the region of the bathymetry slope and need to integrate along depth as coordinate, which is in practice not trivial. Additionally, intervening bathymetry is also a factor of disturbance, e.g. MAR. Pressure values in Equation 3.1 are defined at the basin slope which corresponds to OBP values and these are mainly given as regular or irregular longitude/latitude grids, nevertheless the integration is done in the depth direction. In particular, the position of the bathymetry slope in the grid is hard to link with depth. Given a zonal cross-section for a particular latitude, the corresponding OBP values are uniquely linked to particular longitude values, since each point on the bathymetry corresponds to only one unique longitude. This approach facilitates the encounter of the corresponding slope values. The unique link between OBP and longitude allows the reformulation of Equation 3.1 with Green's theorem (Kvas, 2024). The following derivations are documented and implemented in the Python package *grates* (Kvas, 2024) and are repeated here for the sake of completeness.

In general, Green's theorem gives the relation between a line integral over a closed curve C and the integral over a plain region A constrained by C. It is a special case of the more general Stoke's theorem and is used to convert regional integrals into line integrals and vice versa. Green's theorem states, for two generic functions P and Q in the x- and z-plane, where the ocean basin cross section is defined, that

$$\iint_A \left(\frac{\partial P}{\partial x} - \frac{\partial Q}{\partial z} \right) dx\, dz = \oint_C (P\, dz + Q\, dx) \tag{3.5}$$

whereas x is the longitude in cartesian coordinates and z is the ocean depth. Now if we set $P = p$ with p corresponding to pressure, and $Q = 0$, Equation 3.5 simplifies to,

$$\iint_A \frac{\partial p}{\partial x}\, dx\, dz = \oint_C p\, dz \tag{3.6}$$

Following the concept of geostrophy, the Coriolis force and the pressure gradient force are in approximate balance for midlatitude synoptic-scale motions (Holton and Hakim, 2013). As we are interested in the MT we derive from geostrophy the geostrophic meridional velocity as (Holton and Hakim, 2013),

$$v_y(x, z) = \frac{1}{\rho_0 f_y} \frac{\partial p}{\partial x} \tag{3.7}$$

with f_y corresponding to the Coriolis parameter and y as latitude in Cartesian coordinates. Geostrophy is a key reason for selecting the area of interest starting at 10 °N. In the equatorial region, geostrophic balance fails because the Coriolis force vanishes (Holton and Hakim, 2013). Now we can insert Equation 3.7 into Equation 3.6 which yields,

$$\rho_0 f_y \iint_A v_y(x, z)\, dx\, dz = \oint_C p\, dz \tag{3.8}$$

hence, the cross-section integral over a plain region A of the geostrophic velocity can be expressed as a pressure integral over the boundary of the cross-section C. In Figure 3.4, the plain region A and the corresponding boundary C of the zonal cross-section at 26 °N in the NA for the depth layer between 3000 m and 5000 m are depicted. The boundary C, indicated by a light blue line, constrains the cross-section A between the depths of 3000 m and 5000 m. The issue with the MAR mentioned in section 3.1, acting as intervening topography, is clearly visible here.

In Equation 3.8, the meridional velocity and the integral are presented in Cartesian coordinates, whereas the dataset is provided on a latitude/longitude grid. Considering a zonal ocean cross-section at latitude ϕ, and the identity (Holton and Hakim, 2013),

$$dx = a\, \cos(\phi)\, d\lambda \tag{3.9}$$

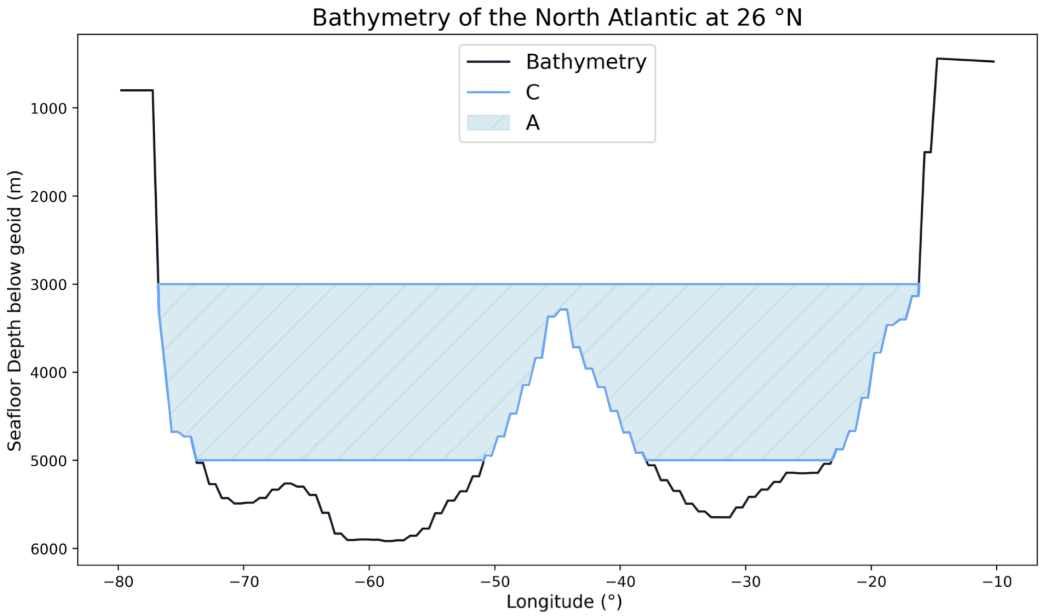


Figure 3.4: Bathymetry of the North Atlantic basin at 26 °N with corresponding plain region A (shaded) and boundary C (blue line) for the depth layer between 3000 m and 5000 m.

one can reformulate the meridional velocity in Equation 3.7 to,

$$v_\phi(\lambda, z) = \frac{1}{\rho_0 \, f_\phi \, a \, \cos(\phi)} \frac{\partial p}{\partial \lambda} \tag{3.10}$$

and Equation 3.8,

$$a \, \cos(\phi) \iint_A v_\phi(\lambda, z) \, d\lambda \, dz = \frac{1}{\rho_0 \, f_\phi} \oint_C p \, dz \tag{3.11}$$

with $a = 6371\,\text{km}$ the Earth's radius. Equation 3.11 and the meridional ocean velocity in Equation 3.10 can be applied to the previous formulation of MT given in Equation 3.1,

$$\Psi_\phi(z) = a \, \cos(\phi) \iint_A v_\phi(\lambda, z) \, d\lambda \, dz = \frac{1}{\rho_0 \, f_\phi} \iint_A \frac{\partial p}{\partial \lambda} \, d\lambda \, dz = \frac{1}{\rho_0 \, f_\phi} \oint_C p \, dz \tag{3.12}$$

The closed curve C, which constrains the plain region A represents the sum of all horizontal components L and the ocean bathymetry B. The number of horizontal components L depends on the depth layer. Upper layers that do not encompass the full range of the ocean floor have two horizontal components. In contrast, deeper layers, where the lower boundary is completely constrained by the bathymetry, have only one horizontal component. For the depth range between 3000 m and 5000 m, C includes two horizontal components, $L(\lambda, z_{\text{min}})$ and $L(\lambda, z_{\text{max}})$, as well as a curve $B(\lambda, z)$, which represents the boundary by the ocean bathymetry, as illustrated in Figure 3.5. As a matter of convenience, from the bathymetry denoted as b, we

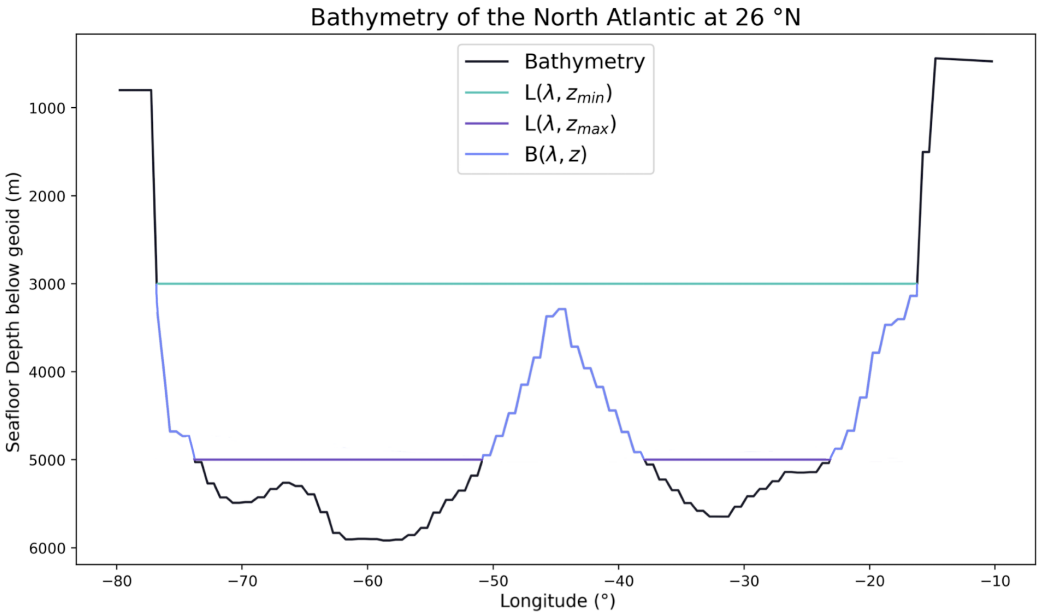


Figure 3.5: Bathymetry of the North Atlantic basin at 26 °N with corresponding horizontal components L and bathymetry B for the depth layer between 3000 m and 5000 m.

introduce the synthetic bathymetry which reads,

$$\tilde{b}(\lambda) = \max\{z_{\min}, b(\lambda)\} \tag{3.13}$$

It describes the depth of the ocean floor at a specific point λ in the zonal cross-section. Hence, the lower boundary curve reads $B(\lambda, \tilde{b}(\lambda))$. Based on these definitions we can split the closed line integral in Equation 3.12 into the integration ranges L and B,

$$\oint_C p\,dz = \underbrace{\int_L p\,dz}_{=0} + \int_B p\,dz \tag{3.14}$$

The integration of L equals zero, as it corresponds to the integral of one or two straight lines, with $dz = 0$. Changes in depth (i.e. slope) along B are determined by the (synthetic) bathymetry $\tilde{b}$ and are given by (Kvas, 2024),

$$dz = \tilde{b}'(\lambda)\,d\lambda \tag{3.15}$$

with $\tilde{b}'(\lambda)$ as the bathymetry slope. Consequently, we can rewrite the equation in terms of λ as

$$\oint_C p\,dz = \int_{\lambda_1}^{\lambda_2} p_\phi\,\tilde{b}'(\lambda)\,d\lambda \tag{3.16}$$

where λ_1 and λ_2 are the zonal extents of the cross-section. Given a zonal ocean cross-section at latitude ϕ, the ocean floor consequently follows the boundary curve B, and thus pressure values at B are OBP values. Furthermore, each depth value corresponds to a unique longitude value, and therefore the gradient of the bathymetry

reads as $\tilde{b}'_\phi(\lambda)$. Regarding the horizontal boundaries L, pressure values are not OBP values. Nevertheless, this does not affect the MT estimation as $dz = 0$ for the upper and lower boundary constrained by z_{min} and z_{max} (see Figure 3.5). Thus, the MT for a zonal ocean cross-section at latitude ϕ can be estimated by simply integrating the product of OBP values and the slope of the bathymetry from the cross-section boundaries λ_1 to λ_2 (Kvas, 2024),

$$\Psi_\phi = \frac{1}{\rho_0 f_\phi} \int_{\lambda_1}^{\lambda_2} \text{OBP}_\phi(\lambda)\, \tilde{b}'_\phi(\lambda)\, d\lambda \tag{3.17}$$

Comparing Equation 3.17 with the initial MT estimation by Equation 3.1 yields a significantly easier and more comfortable approach in terms of calculation. The issue of locating λ_1 and λ_2 is dealt with as mentioned before, as each OBP value corresponds to a unique longitude. In further analysis, we are interested in dealing with depth layers, constrained by z_{min} and z_{max}. To incorporate this into the integration seen in Equation 3.17, a so-called window function is introduced,

$$\delta_\phi(\lambda) = \begin{cases} 1 & \text{if } z_{\text{min}} \leq z(\lambda) \leq z_{\text{max}} \\ 0 & \text{otherwise} \end{cases} \tag{3.18}$$

The window function is one if the longitude is within a certain depth layer constrained by z_{min} and z_{max} and zero if not. With the window function, the estimation of MT for a given zonal ocean cross-section reads,

$$\Psi_\phi = \frac{1}{\rho_0 f_\phi} \int_{\lambda_{\text{min}}}^{\lambda_{\text{max}}} \delta_\phi(\lambda)\, \text{OBP}_\phi(\lambda)\, \tilde{b}'_\phi(\lambda)\, d\lambda \tag{3.19}$$

Equation 3.19 exhibits the capability of estimating the MT of a given ocean basin cross-section at latitude ϕ and depth layer, solely by integrating the product of OBP and bathymetry slope along the basin extent constrained by λ_{min} and λ_{max}.

Another important estimate is the stream function of the AMOC, which can be derived from Equation 3.19. The stream function ζ_ϕ is given as the cumulative integral of the MT for a certain zonal cross-section and reads (McCarthy et al., 2015),

$$\zeta_\phi(z) = \int_{z=0}^{z_{\text{max}}} \Psi_\phi(z) \tag{3.20}$$

The maximum of the stream function $\max(\zeta_\phi(z))$ is crucial for estimating the state of the AMOC as it corresponds to its strength. It is an important indicator of AMOC change and the mean state of the overturning (McCarthy et al., 2015).

3.3 Meridional Transport via Ocean Velocity

A crucial step to validate the estimated cross-basin MT by OBP in Equation 3.19 is to use OVEL data and integrate them over the plain region A, as seen in Figure 3.4. We start again with Cartesian coordinates and therefore the MT at latitude y with meridional ocean velocity v_y reads,

$$\Psi_y = \iint_A v_y(x,z)\,dx\,dz = \int_x \int_z v_y(x,z)\,dx\,dz \tag{3.21}$$

The integral over the plain region A can be expressed as an integral along x (longitude) and z (depth). For a given zonal cross-section at ϕ and by using the identity in Equation 3.9, the integral in Equation 3.21 can be reformulated to spherical coordinates as,

$$\Psi_\phi = a\,\cos(\phi) \int_\lambda \int_z v_\phi(\lambda,z)\,d\lambda\,dz \tag{3.22}$$

with λ being the longitude, z the depth below the surface, v_ϕ the meridional velocity of the ocean water, $a = 6371\,\mathrm{km}$ the Earth's radius, and ϕ the latitude. Care must be taken during the integration due to the discrepancy in units between λ (degrees) and z (meters). In the context of this study, we are examining constant latitudes, which means we have fixed zonal cross-sections of the Atlantic basin. Thus, we only consider changes in longitude ($\Delta\lambda$) at a fixed latitude (ϕ = const.). As we integrate along longitude, we need the distance between two neighboring points. The distance between these two points in degrees is given as $\Delta\lambda$. The use of $\cos(\phi)$ scales the Earth's radius to account for the decrease in distance covered per degree of longitude as you move from the equator to the poles. As a change of longitude ($\Delta\lambda$) at constant latitude on the Earth's surface is described via the arc length s_ϕ, we can formulate it as,

$$s_\phi(\lambda) = a\,\cos(\phi)\Delta\lambda \tag{3.23}$$

With the use of the arc length in Equation 3.23, accounting for a change in distance due to a change in longitude at certain latitude, the meridional transport Ψ_ϕ can be calculated by considering the integral over the velocity field v_ϕ along the longitude and depth as,

$$\Psi_\phi = \int_{\lambda_1}^{\lambda_2} \int_{z_1}^{z_2} s_\phi(\lambda)\,v_\phi(\lambda,z)\,d\lambda\,dz \tag{3.24}$$

where λ_1 and λ_2 are the bounds of the longitude integration, and z_1 and z_2 are the bounds of the depth integration, corresponding to the closed line C, as seen in Figure 3.4. This formulation ensures that the distance per degree of longitude is correctly scaled by $\cos(\phi)$, reflecting the actual physical distance on the Earth's surface. The primary advantage of such a linearized distance calculation in longitude is its computational efficiency and simplicity. While it's true that the Earth's radius decreases with increasing ocean depth, making the distance between two points due

to a change in longitude slightly smaller, this effect is negligible at synoptic scales. The increase in depth is minor compared to the Earth's radius, allowing us to safely disregard this consideration. It's also important to note that the Earth is a geoid rather than a perfect sphere. Although this analysis does not account for this, future studies may incorporate the Earth's geodetic shape for more precise calculations.

As we have now accounted for the change in distance between two points at a constant latitude on the Earth's surface, we can rewrite Equation 3.24 with the window function $\delta_\phi(\lambda)$ formulated in Equation 3.18 to,

$$\Psi_\phi = \int_{\lambda_{\text{min}}}^{\lambda_{\text{max}}} \int_{z_{\text{min}}}^{z_{\text{max}}} s_\phi(\lambda)\, \delta_\phi(\lambda)\, v_\phi(\lambda, z)\, d\lambda\, dz \tag{3.25}$$

To conclude, given a zonal cross-section of the Atlantic basin at latitude ϕ, constrained by $\lambda_{\text{min}}/\lambda_{\text{max}}$ and $z_{\text{min}}/z_{\text{max}}$, one can estimate the MT by integrating the product of meridional OVEL, arc length s_ϕ, and depth window δ_ϕ along longitude and depth. This method provides a valuable opportunity to validate the MT estimation using OBP as described in Equation 3.19.

3.4 RAPID

A special location to monitor the variability of the AMOC is at 26 °N. The project known in this context is the so-called Rapid Climate Change-Meridional Overturning Circulation and Heatflux Array (RAPID) (Moat et al., 2023). It is a collaborative project between the National Oceanographic Center (Southampton, U.K.) and the National Oceanic and Atmospheric Administration (NOAA) (McCarthy et al., 2015). The goal of RAPID is to measure and monitor directly the AMOC and OHC across the latitude of 26 °N for the whole depth range (Moat et al., 2023). An interesting remark is that in this region of latitude also the Subtropical Gyre, mainly driven by ET, is apparent. The in-situ measurements began in April 2004 and have continued until present (Moat et al., 2023). The purpose is to deliver a continuous time series of transbasin MT between the Bahamas and the Canary Islands and to combine it with the flux through the Florida Straits (FS) (Frajka-Williams, 2015). The basic principle of the MT estimation from RAPID data is geostrophy (McCarthy et al., 2015). Geostrophic MT from RAPID data was calculated via the Thermal Wind Balance according to McCarthy et al. (2015).

Between the Bahamas and the Canary Islands mooring arrays are deployed, whereas in the FS cable measurements are used (Frajka-Williams, 2015). Figure 3.6 gives an overview of the RAPID location in the NA (Moat et al., 2020). As previously mentioned, the array traverses through the Subtropical Gyre of the NA, providing valuable insights into the Ekman-forced surface transports responsible for the for-

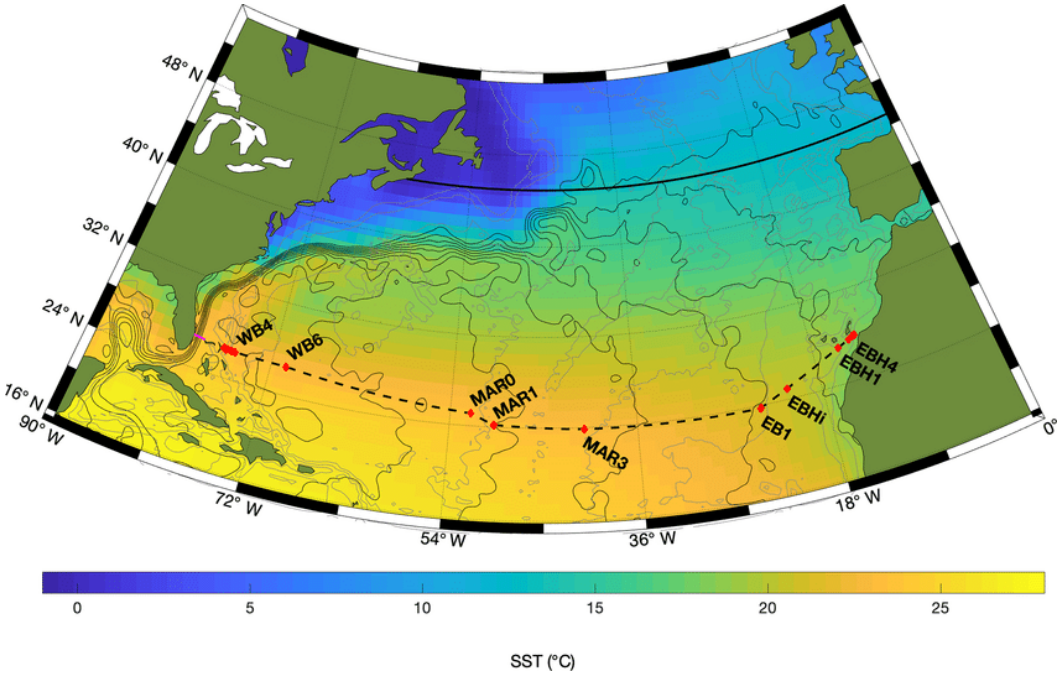


Figure 3.6: RAPID location and SST averaged from 1999 to 2018 in the North Atlantic. Black lines correspond to sea surface height contours (interval 0.1 m) (Moat et al., 2020); licensed by CC BY 4.0.

mation and maintenance of the Subtropical Gyre (see section 2). Red diamonds interconnected by a dashed black line indicate the position of the moorings. The MAR at 26 °N is located at approximately 45 °W, hence "WB", "MAR" and "EB" denote, respectively, moorings in the Western Basin-, MAR-, and Eastern Basin Region (Moat et al., 2023). It is to be mentioned that not all moorings are listed here for clarity. Narrow sea surface height contours near the west coast and wide contours near the east coast indicate strong and narrow Western Boundary Currents and smooth and wide Eastern Boundary Currents, respectively (see section 2.2). Taking into account the Trade Winds near the equator and the Westerly Winds at mid-latitudes, one can deduce the location of the Subtropical Gyre in this region. Concerning Figure 3.7, in red are shown warm surface currents like the Gulf Stream, North Atlantic Current (NAC), Labrador Current (westward extension of the NAC), and Norwegian Current (eastward extension of NAC) (Buckley and Marshall, 2016). Indicated in blue are the deep and cold ocean currents, like the Deep Western Boundary Current. Figure 3.7 emphasizes the importance of the chosen location for the RAPID array, as all major upper and lower ocean currents traverse through this region. Moorings are distributed along 26 °N covering the whole depth range of the NA basin in this region, as seen in Figure 3.7. As a matter of clarity, again, not all moorings are listed here.

Mounted onto the moorings are different measurement instruments like Conductivity-Temperature-Depth (CTD) sensors for salinity, temperature, and depth or Moored

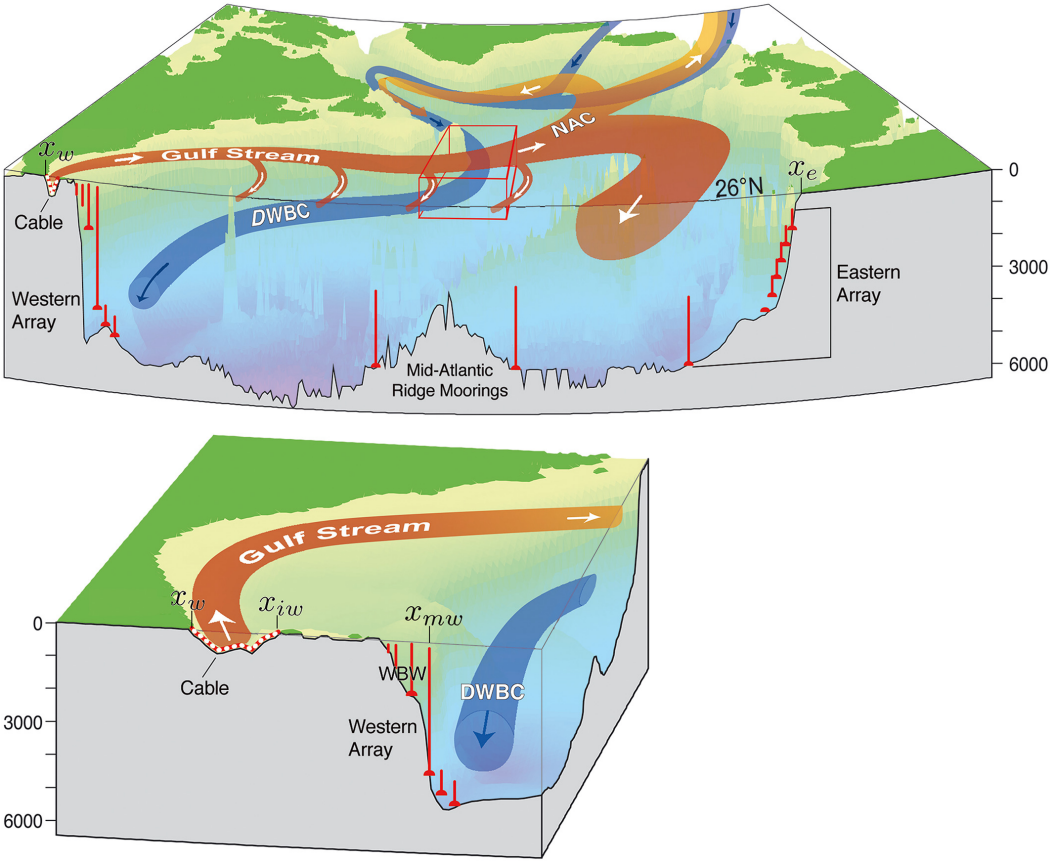


Figure 3.7: Cross Section of the North Atlantic Basin at 26 °N which corresponds to the RAPID location. Warm surface currents are shown in red, while cold deep ocean currents are depicted in blue (Buckley and Marshall, 2016); licensed by CC BY-NC-ND 4.0.

Inverted Echo Sounders (MIES) to measure the trip travel time of acoustic signals for the estimation of the temperature structure of the water column over time (Moat et al., 2023). All of these instruments help to get a better understanding of the AMOC and its variability. The RAPID project is fundamental for the enhancement of the understanding of oceanographic processes, especially the monitoring of AMOC variability, and also a necessity for further analysis in the context of this study. The mooring arrays provide direct, in-situ measurements of oceanic properties, serving as reference data to validate the estimation of NA cross-section MT by Equation 3.19. With its high-frequency data collection (half-daily sampling), the project captures short-term variability and seasonal changes that might be overlooked by model and satellite data. In addition, RAPID monitors the entire water column, providing depth-specific insights that are crucial for understanding the role of deep ocean currents in global heat and carbon distribution (Moat et al., 2023). The array's continuous monitoring across the Atlantic at 26 °N allows for observing long-term trends and obtaining a comprehensive cross-sectional view of transatlantic oceanic flows. This combination of depth, precision, and temporal resolution make RAPID a

vital complement to other data sources, like reanalysis and satellite data, significantly improving precision in evaluating the state of the AMOC at 26 °N.

3.4.1 RAPID Data

Data from the RAPID AMOC monitoring project is funded by the Natural Environment Research Council (United Kingdom) and is freely available from `www.rapid.ac.uk/rapidmoc` (last accessed on 19 May 2024). The period used is from 2004-04-01 to 2022-02-02 and the data are given as half-daily values (Moat et al., 2023). Due to the full zonal extent of the RAPID array in the NA, data gaps due to damage from fishing vessels (mainly trawlers) were apparent in the data. These gaps were interpolated according to Moat et al. (2023). The datasets used in this work are *moc_transports* and *moc_vertical*, which are in NetCDF format and were initially resampled to a monthly means time series. The file *moc_transports* comprises MT for certain components of the AMOC and layer transports which are given for certain depth layers (Moat et al., 2023). On the other hand, the file *moc_vertical* contains the vertical profile of the overturning stream function at each time, i.e. MT given for the whole depth range and observational period (Moat et al., 2023). The transport itself is given in Sv (1 Sv = 10^6 m^3/s) and positive transport values correspond to northward flow and vice versa (Moat et al., 2023). The individual components in *moc_transports* are listed in Table 3.1.

Table 3.1: Variables in *moc_transports* RAPID data.

Transport Type	Depth Category	Identifier
Meridional Overturning Circulation	-	MOC
Upper Mid-Ocean	-	UMO
Florida Straits	-	FS
Ekman	-	EK
Thermocline Recirculation	0 m to 800 m	TR
Intermediate Water	800 m to 1100 m	IW
Upper North Atlantic Deep Water	1100 m to 3000 m	UNADW
Lower North Atlantic Deep Water	3000 m to 5000 m	LNADW
Antarctic Bottom Water	below 5000 m	ABW

The first component `MOC` corresponds to the total northward transport of the AMOC, i.e. the sum of all water masses heading north which is denoted as Meridional Overturning Circulation (MOC). Terms `UMO`, `FS` and `EK` correspond to component transport of the MOC and are specified as Upper-Mid-Ocean (UMO), FS and ET respectively. The remaining components, `TR`, `IW`, `UNADW`, `LNADW` and `ABW` are layer transports classified via their depth ranges. The nomenclature and classification of

the MT seen in Table 3.1 will be pursued and adhered to in the further course of this analysis to guarantee comparability between the data product estimations.

3.5 ECCO

The ECCO project stands for a collaborative research effort aimed at producing the most accurate possible estimates of the climatic state of the global ocean for a better understanding of the ocean's part in the global climate system (ECCO-Consortium et al., 2021b). ECCO's approach is to assimilate observational data into model simulations in a framework called state estimation. Hence, it is a reanalysis model (ECCO-Consortium et al., 2021b).

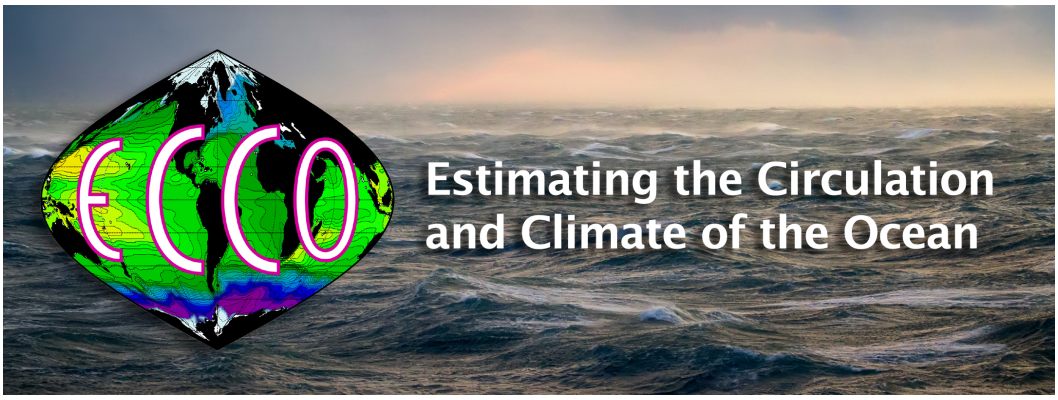


Figure 3.8: Estimating the Climate and Circulation of the ocean (ECCO) logo (ECCO-group, 2024).

3.5.1 ECCO Data

In the framework of this study, the ECCO Version 4 Release 4 (ECCO V4R4) is used (ECCO-Consortium et al., 2021b). ECCO V4R4 represents the latest advancement of the global ocean state estimate by ECCO-Consortium et al. (2021b). This release extends the analysis period from 1992 to 2017, which corresponds to the altimetry era and integrates a wide array of observational data with the Massachusetts Institute of Technology general circulation ocean model (MITgcm). The dataset has been expanded to include a wider range of observational data, now featuring updated satellite altimetry and various in situ measurements (Forget et al., 2015).

Observational data conditions used in ECCO V4R4 are Sea Surface Height (SSH) from satellite altimetry (TOPEX, ENVISAT), SST and SSS from satellite radiometers and scatterometers (AVHRR, Aquarius), OBP from satellite gravimetry (Gravity Recovery and Climate Experiment (GRACE)) and ocean temperature and salinity with CTD sensors and Expandable Bathy-Thermographs (XBT) from a couple of

programs (WOLE, ARGO, etc.) (Forget et al., 2015). These enhancements are designed to refine the model's input data quality and coverage, ensuring a more accurate reflection of the real-world ocean state. Incorporation of in-situ data into a model is therefore crucial, as it represents to some extent the reference. Significant improvements in R4 include the use of nonlinear free surface formulation and real freshwater flux boundary conditions, enhancing the model's ability to simulate sea level changes more accurately (ECCO-Consortium et al., 2021b).

ECCO V4R4 is accessible via the NASA Physical Oceanography Distributed Active Archive Center (PODAAC) under `https://podaac.jpl.nasa.gov/` (last accessed on 19 May 2024). In the context of this work, the ECCO products OBP, OVEL and ocean geometry are used. As mentioned above, the period ranges from 1992 to 2017 and therefore covers the whole altimetry era. Both products are given on a longitude/latitude grid with a resolution of 0.5° x 0.5°. OBP values are given for the ocean bathymetry, i.e. there is no depth coordinate (ECCO-Consortium et al., 2021a) and are used to estimate the MT anomalies following Equation 3.19. To incorporate ocean bathymetry, i.e., depth, into the dataset, the OBP data was combined with the ocean geometry to create a single, integrated dataset. On the other hand, the OVEL data is also resolved in depth dimension with a decreasing resolution with increasing ocean depth (Fenty and Wang, 2020) and used to cross-validate the estimated MT anomalies by OBP by the use of Equation 3.25.

According to ECCO-Consortium et al. (2021a), OBP omits the influence of global mean atmospheric pressure, making it appropriate for comparison with GRACE data products (ECCO-Consortium et al., 2021a). According to the documentation of the ECCO-Consortium et al. (2021a), the OBP is calculated via first estimating the ocean hydrostatic bottom pressure anomaly, denoted as PHIBOT, and is defined by,

$$\text{PHIBOT} = \frac{p_b}{\rho_0} - gH(t) \tag{3.26}$$

where p_b represents the model ocean hydrostatic bottom pressure, ρ_0 is the reference density set to 1029 $\mathrm{kg/m^3}$, g is the gravitational acceleration with 9.81 $\mathrm{m/s^2}$, and $H(t)$ is the depth of the model at time t. Subsequently, the OBP is given by (ECCO-Consortium et al., 2021a),

$$\text{OBP}_h = \frac{\text{PHIBOT}}{g} + \text{corrections} \tag{3.27}$$

Resulting OBP values from Equation 3.27 are given in meters of equivalent water thickness (m) and can be transformed via the hydrostatic pressure equation into Pascals (Pa),

$$\text{OBP}_p = \rho_0 \, g \, \text{OBP}_h \tag{3.28}$$

whereas OBP_h corresponds to the OBP in equivalent water thickness and OBP_p as OBP given in Pascal. The corrections in Equation 3.27 include (ECCO-Consortium et al., 2021a), adjustments concerning global mean steric sea level changes resulting from density variations in the Boussinesq volume-conserving model, known as the Greatbatch correction, and adjustments for variations in global mean atmospheric pressure.

3.6 GRACE/GRACE-FO

The Gravity Recovery and Climate Experiment (GRACE) mission started in March 2002 and finished in October 2017 (Tapley et al., 2004; Kornfeld et al., 2019). As its successor, Gravity Recovery and Climate Experiment - Follow On (GRACE-FO) was initialized in May 2018, featuring higher spatial accuracy, better altitude resolution, less fuel consumption, and new technology such as a laser ranging interferometer (LRI) for improved precision in measuring the space between the satellites (Kornfeld et al., 2019; Landerer et al., 2020). GRACE/GRACE-FO, in general, is a collaborative effort between NASA and the German Aerospace Center (Deutsche Luft- und Raumfahrtbehörde) to map Earth's gravitational field with unprecedented detail (Tapley et al., 2004). GRACE/GRACE-FO is using two equal satellites, GRACE-A and GRACE-B, which fly 220 km apart in a near-polar orbit (Adam, 2002). The main objective is to detect anomalies in Earth's gravitational field by monitoring the distance between the satellites using a microwave ranging system and GPS technology (Adam, 2002; Kornfeld et al., 2019). GRACE/GRACE-FO is capable of detecting geoid height changes as small as 2 mm to 3 mm with a spatial resolution of approximately 300 km (Tapley et al., 2004; Landerer et al., 2020). Gravity anomalies emanate from the redistribution of mass in the Earth's system, i.e. water, ice sheets, or land mass. To date, GRACE/GRACE-FO has provided invaluable data, enhancing our understanding of Earth's water cycle, ice mass changes, and sea level variations (Landerer et al., 2020). For instance, the data has been instrumental in tracking changes in terrestrial water storage, monitoring groundwater depletion, and studying the melting of polar ice (Adam, 2002; Tapley et al., 2004). Due to its high sensitivity to gravity anomalies, GRACE/GRACE-FO enables investigations into ocean currents, such as those in the AMOC system. GRACE/GRACE-FO delivers updated gravity maps every thirty days, offering a dynamic view of Earth's gravity field rather than a static one (Landerer et al., 2020).

The mass of components like ice sheets, land water storage, or water mass in the Atlantic basin cannot be directly estimated with the GRACE/GRACE-FO satellites. GRACE/GRACE-FO can only detect variations, i.e., anomalies, and cannot distinguish between different sources of mass (Tapley et al., 2004). Therefore, when comparing MT estimations in between various data products such as RAPID, ECCO,



Figure 3.9: GRACE-FO assembly at Harris Spaceport Systems facility at Vandenberg Air Force Base in California (NASA, 2024a) and illustration of the twin spacecraft GRACE-A and GRACE-B (NASA, 2024b).

or GRACE/GRACE-FO, we utilize anomalies. The only exception is the analysis of MT estimation solely by RAPID data. Concerning GRACE/GRACE-FO, to obtain absolute MT values in the Atlantic basin, an Earth model containing information on the actual mass state of the NA would be required. On short time scales, mass anomalies in the ocean are solely influenced by the redistribution of water in both solid and liquid forms, which consequently, in liquid form, alters the AMOC. Mass redistributions in the lithosphere occur over much longer time scales and are therefore not considered.

3.6.1 Synthetic GRACE/GRACE-FO data

In this work, we use synthetic GRACE/GRACE-FO data rather than real GRACE/GRACE-FO observations. This allows us to make initial comparisons and establish a framework for the future integration of real GRACE/GRACE-FO observations. This approach entails incorporating realistic GRACE/GRACE-FO-like noise into ECCO OBP data and subsequently applying filtering techniques to generate synthetic GRACE/GRACE-FO data. The synthetic GRACE/GRACE-FO dataset will span the entire available period which coincides with the ECCO data, from January 1992 to December 2017, thus covering the complete ECCO time period for better comparability and consistency. It should be noted that, of course, real GRACE/GRACE-FO data only starts from March 2002, however, this synthetic approach allows us to create a comprehensive time series spanning the full duration of the ECCO data (1992 until 2017). The creation of synthetic data is essential for the validation and enhancement of GRACE/GRACE-FO data processing methodologies, providing a framework for the use of real GRACE/GRACE-FO data. The overarching objective of

future research in this context, is to estimate MT using solely OBP anomalies derived from real GRACE/GRACE-FO observations.

The procedure for generating synthetic GRACE/GRACE-FO data is as follows. Initially, the OBP data from ECCO, provided on a global grid with a resolution of 0.5° x 0.5°, serves as the base dataset. To introduce noise with realistic error characteristics for each month, the Normal Equation Matrix is employed. This is followed by the application of Cholesky decomposition to decompose the Normal Equation Matrix into a lower triangular matrix, facilitating the creation of a correlated noise vector. For each month in the ECCO OBP dataset, a new spherical harmonic noise vector is generated, simulating the measurement errors typically observed in GRACE/GRACE-FO data. The ECCO OBP data is then transformed into spherical harmonic coefficients up to degree and order 96. The spherical harmonic noise vector for each month is added to the corresponding ECCO OBP data. At this stage, the data closely resembles raw GRACE/GRACE-FO data, where the noise magnitude significantly exceeds the actual signal. Consequently, a spatial filter is applied to the combined spherical harmonic coefficients (ECCO OBP + noise) to replicate the spatial filtering utilized in GRACE/GRACE-FO data processing (Kusche et al., 2009). Following this filtering, the spherical harmonic coefficients are converted back into a longitude/latitude grid, resulting in a synthetic GRACE/GRACE-FO OBP dataset. This summarizes the process of generating synthetic GRACE/GRACE-FO data utilized in this study.

4 Results

4.1 Meridional Transport Estimation from RAPID at 26 °N

The MT estimations in this section adhere to the transport definitions provided in Table 3.1. Transport values are analyzed, as opposed to transport anomalies, which will be addressed in section 4.2 and section 4.3. Not all components as listed in Table 3.1 are of interest, as also further discussed and explained in section 4.2. All estimations were derived from RAPID data, hence at 26 °N. To recap, positive MT values correspond to northward transport, whereas negative values correspond to southward transport. Figure 4.1 presents the time series and monthly means of the meridional component transports for the MOC, FS, and ET. These components are critical for understanding the dynamics and variability of the AMOC, as discussed in section 2.3. Similarly, Figure 4.2 displays the time series and monthly means of the meridional layer transports for the Lower North Atlantic Deep Water (LNADW) and Antarctic Bottom Water (ABW), corresponding to the depth layers '3000 m to 5000 m' and 'below 5000 m', respectively.

In both figures, the left column illustrates the time series of monthly MT, while the right column shows the monthly mean MT transport over the period from April 2004 to February 2022. The original monthly time series is depicted by a light blue line, capturing the high-frequency intraannual variations and short-term fluctuations in transport values. A Butterworth filter was applied to the original time series to perform low-pass filtering, shown by a navy blue line to emphasize the long-term trend of the components and reduce intraannual variability. This filtering process helps in identifying underlying trends and patterns that are not immediately apparent in the raw data. The mean of the time series from April 2004 to February 2022 is represented by a light gray line, providing a baseline for assessing deviations and anomalies. Additionally, a linear trend (monthly), estimated using least squares regression, is indicated by an orange line. This linear trend line is essential for understanding the overall direction and rate of change in the transport values over the study period. Both the component and layer transports exhibit large variability over the whole observed period. This variability is indicative of the dynamic and complex nature of the ocean circulation system, influenced by various factors such

as wind stress, change in buoyancy, and basin-scale pressure gradients. Furthermore, each transport indicates strong seasonality. Understanding these seasonal cycles is crucial for predicting short-term changes in the AMOC and its associated climate impacts. This will be further discussed in section 5.

The statistics of the individual component and layer transports are summarized in Table 4.1. This approach helps in analyzing potential changes or shifts in the transport patterns over a longer timescale. All transports, except the LNADW in Table 4.1, are heading north, as indicated by the overall positive mean transports.

Table 4.1: Mean, linear trend (Lin. Trd.) and standard deviation (σ) of RAPID component and layer transports at 26 °N.

Transport	Depth	Mean (Sv)	Lin. Trd. (Sv/decade)	σ (Sv)
MOC	-	16.74	-1.35	2.32
FS	-	31.29	-0.42	1.29
EK	-	3.74	0.29	1.09
LNADW	3000 m to 5000 m	-5.76	0.95	1.53
ABW	below 5000 m	1.06	0.22	0.30

Another key quantity for qualitatively evaluating the state of the AMOC is the stream function ζ. Figure 4.3 illustrates the stream function (left) and the Depth of Maximum Overturning (DMO) (right) at 26 °N derived from the RAPID array. The stream function ζ, increases with depth. This is because it represents the cumulative integral of the cross-sectional MT over the depth direction, effectively capturing the vertical structure of the MT (refer to Equation 3.20). At a certain depth, ζ reaches its positive maximum, which signifies the DMO. This depth corresponds to the peak northward transport often referred to as the MOC. The location of this depth is crucial as it indicates the maximum of northward MT.

Beyond this DMO, the stream function begins to decrease, indicating that the northward transport predominantly occurs in the upper 1000 m of the NA. The decline in ζ with further depth highlights the diminishing influence of northward currents and the increasing role of southward return flows at greater depths. The cumulative integral of cross-sectional MT over the entire depth range, denoted as $\zeta(z_{\max})$, encapsulates the total transport of water masses within the NA, i.e. the closure. Figure 4.3 (left panel) shows that the stream function ζ declines after reaching the DMO and approaches approximately zero at the maximum depth. This behavior suggests that the MT of water masses in the NA basin is effectively closed, with minimal net transport at the greatest depths.

The time series of the DMO (Figure 4.3 right panel) captures the temporal variability of the depth at which maximum northward transport occurs. To emphasize long-term trends, a low-pass filter was applied to the data, with the filtered DMO displayed by a dark blue line. The mean DMO, indicated by a red line, is calculated to be $d_{\mathrm{MOC}} = 1017.6$ m. Both the stream function and the DMO exhibit significant variability over the entire observational period. These variations are indicative of dynamic changes in the strength and pattern of the AMOC, influenced by factors such as variability in surface buoyancy, wind-forcing, and possibly climatic shifts. This variability and its implications for the AMOC will be further discussed in section 5.

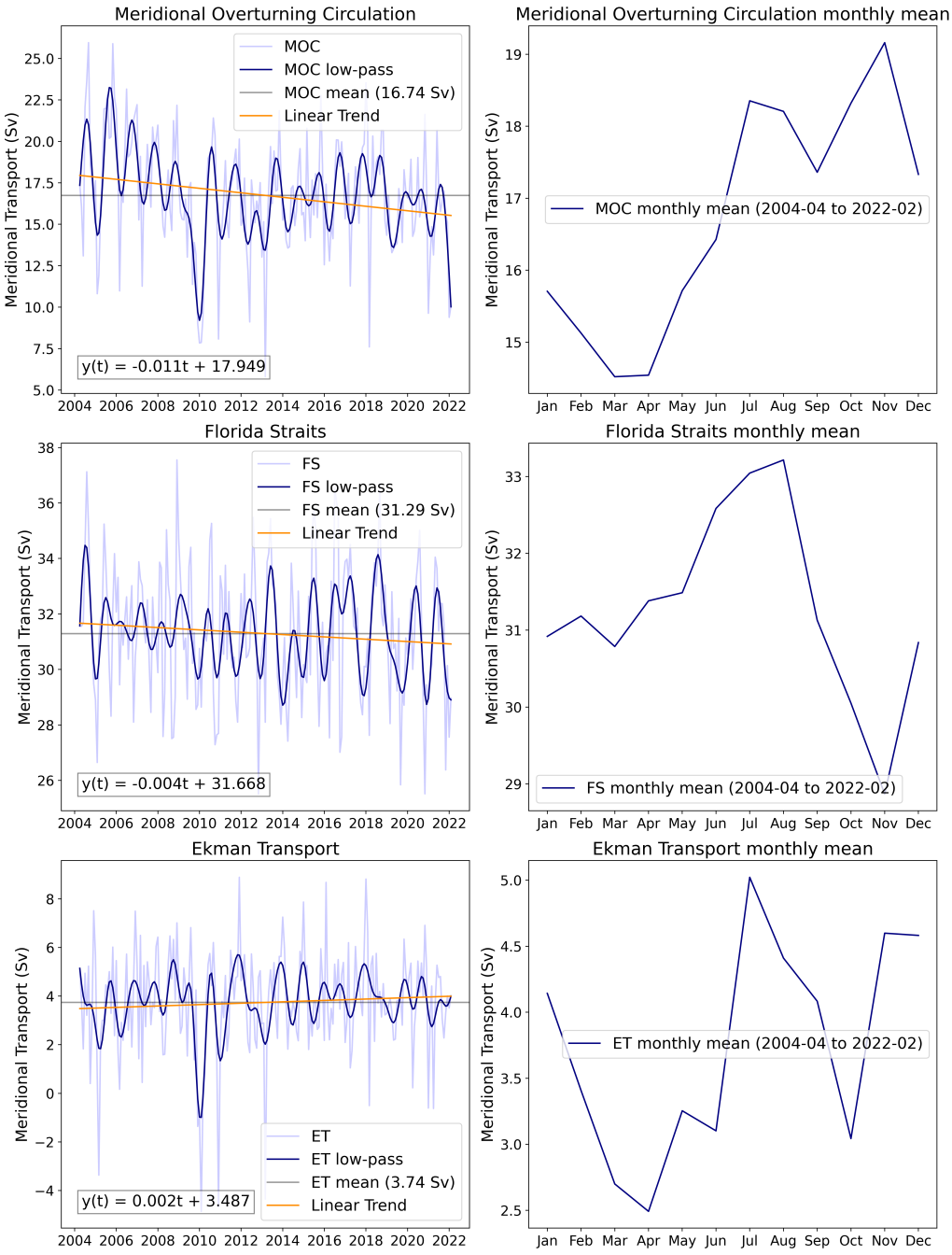


Figure 4.1: Meridional component transports for MOC (top), FS (middle), ET (bottom) from RAPID at 26 °N for monthly time series (left) and the climatological monthly mean (right) over the period 2004-04 to 2022-02.

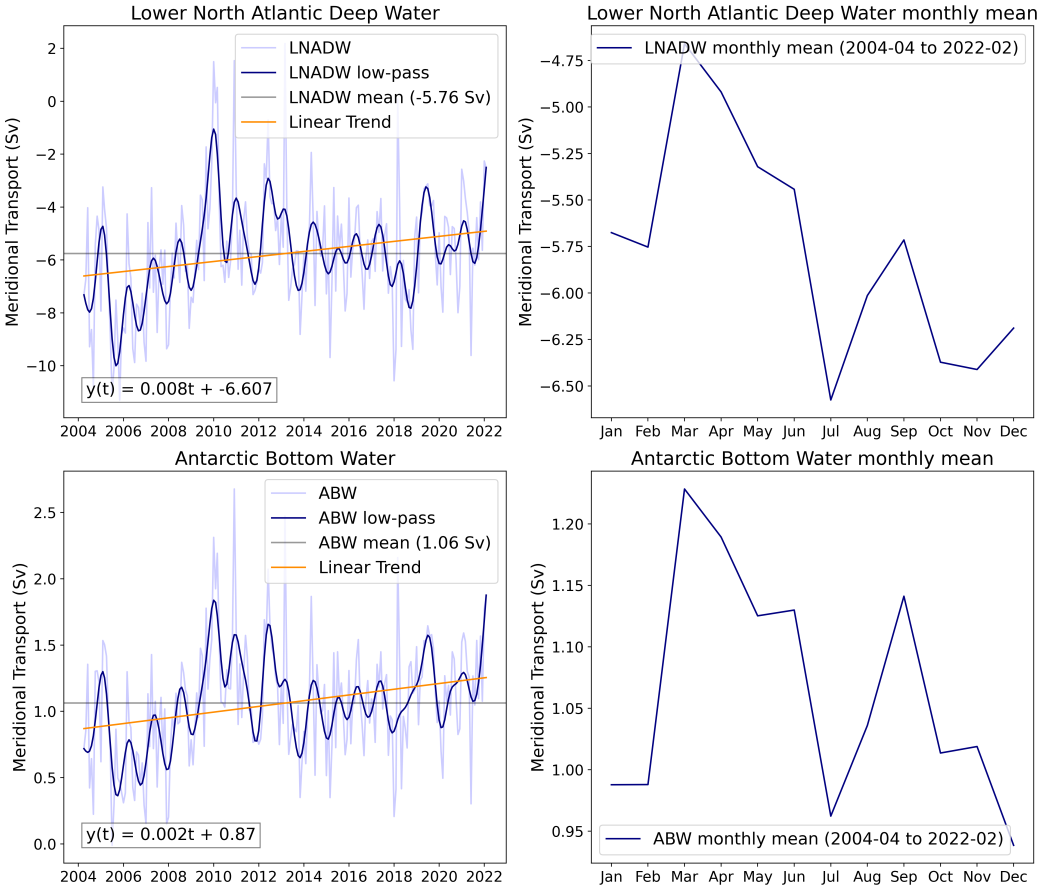


Figure 4.2: Meridional layer transports for LNADW (top) and ABW (bottom) from RAPID at 26 °N for monthly time series (left) and the climatological monthly mean (right) over the period 2004-04 to 2022-02.

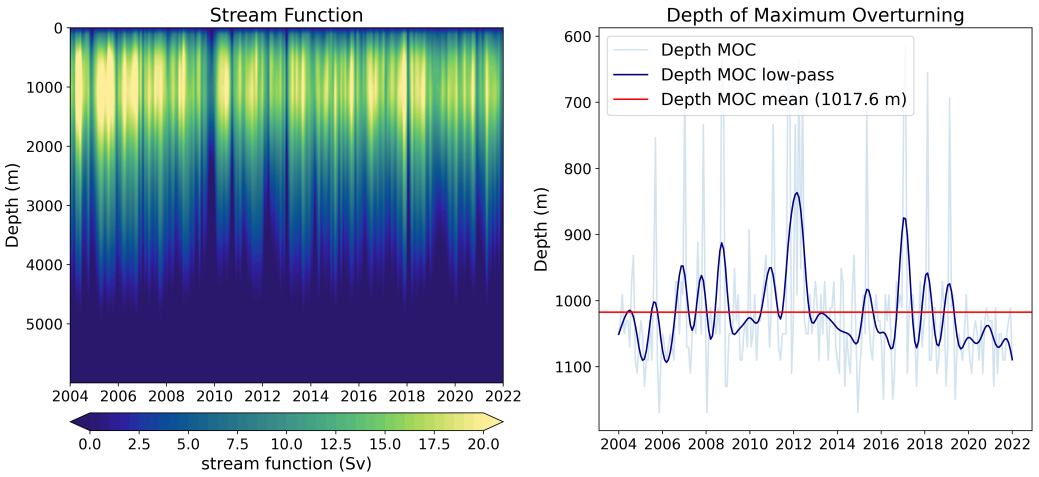


Figure 4.3: Streamfunction and Depth of Maximum Overturning from RAPID at 26 °N for 2004-04 to 2022-02.

4.2 Validation of Meridional Transport Anomaly Estimation from ECCO

The ECCO data provides an opportunity to expand the spatially restricted analysis by RAPID, to the entire Atlantic basin. In this section, we only consider anomalies, which represent deviations from the mean. The cross-sectional MT estimated from RAPID in section 4.1 is now converted to anomalies for better comparability. All of the analyzed data products (RAPID, OBP, and OVEL) have been deseasonalized and detrended to obtain an accurate estimate of the pure anomaly contained within. This process is essential as it removes seasonal variations and long-term trends, allowing for a clearer identification and analysis of significant deviations or anomalies from the expected patterns.

Initially, it is essential to get an overview of the bathymetry of the region of interest. Figure 4.4 shows cross-sectional bathymetries between 10 °W and 80 °W of the NA along the entire extent of the area of interest, ranging from 10 °N to 66.5 °N. A uniformly distributed step size of 8 ° was chosen to display the change in bathymetry at higher latitudes. Figure 4.4 shows that the bathymetry of the NA becomes shallower with increasing latitude. This is confirmed by Figure 4.5, which displays the mean longitudinal bathymetry over latitude indicated by a dark gray line. The bathymetry becomes significantly shallower towards the north, especially near the continental shelf of Greenland at around 58 °N. The distribution of depth values along the longitude is crucial for assessing the estimation of cross-sectional MT by Equation 3.19. This is because the distribution of depth values in the ECCO dataset also indicates the distribution of OBP values on the bathymetry. As mentioned in section 3.2, for a given zonal cross-section at latitude ϕ, each OBP value on the bathymetry corresponds to a unique longitude. Since each longitude is only represented once in every zonal cross-section, every longitude value and therefore each OBP value corresponds to one unique depth value on the ocean bathymetry.

To understand the distribution of depth values on the bathymetry according to the depth layer categories in Table 3.1, a histogram is shown in Figure 4.6. The further south the latitude, the more depth values are distributed in the deeper layers; conversely, the further north the latitude, the more depth values are distributed in higher layers. This is clearly visible in the layer between '0 and 800 m' for the latitude of 66 °N, as most of it already belongs to the continental shelf of Greenland. Excluding the very high latitudes like 66 °N and 58 °N, where most values correspond to the Greenlandic Shelf, the layers '3000 m to 5000 m' and 'below 5000 m' contain the most depth (OBP) values along their bathymetry. As previously mentioned, the quality of the MT estimation by Equation 3.19 primarily depends on the distribution of OBP values along the bathymetry. Therefore, the more OBP values are distributed

along the bathymetry, the better the MT estimation. Another significant influence is the slope of the bathymetry. As seen in Figure 4.4, the slopes of the higher layers, i.e., above 3000 m in depth, are very steep, leading to a distorted distribution of OBP values on the bathymetries. Thus, the number of OBP values distributed along the bathymetry in these steep regions is small compared to the depth increase. Consequently, the depth layers '3000 m to 5000 m' and 'below 5000 m', which correspond to the LNADW and the ABW, respectively, are chosen for further analysis.

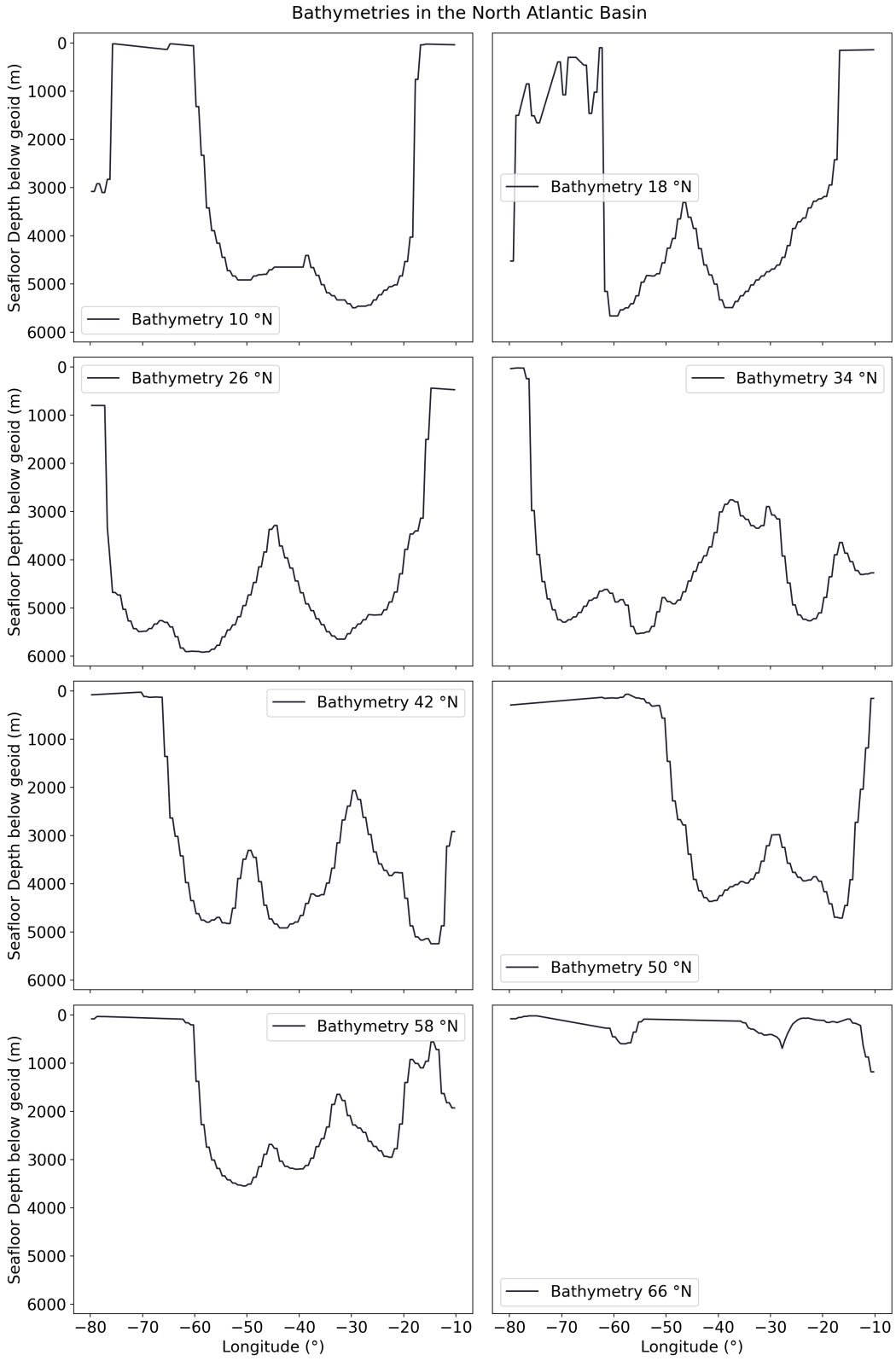


Figure 4.4: Bathymetries in the North Atlantic basin for specific latitudes from ECCO.

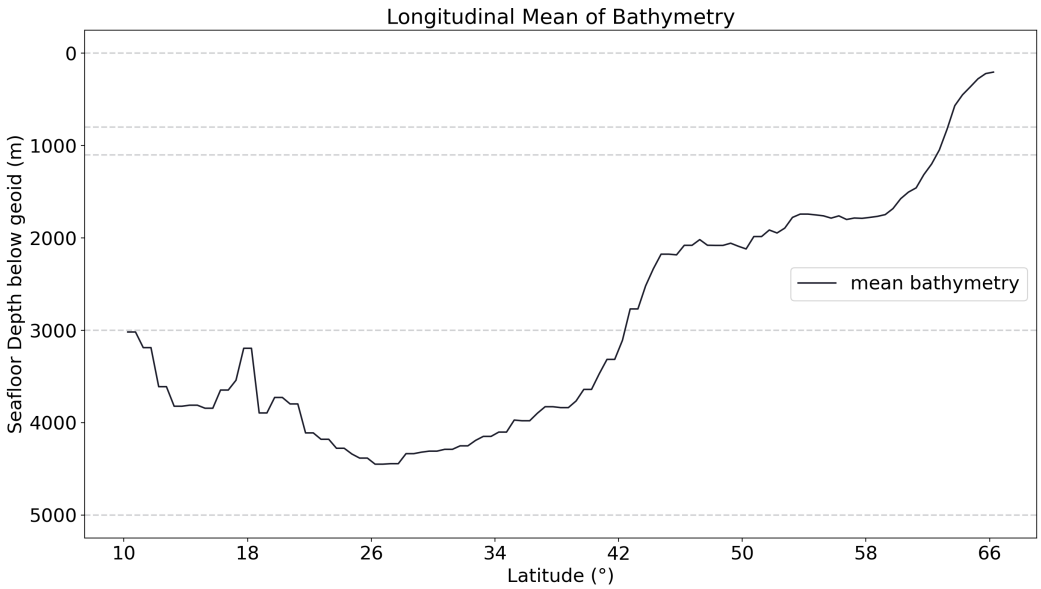


Figure 4.5: Longitudinal mean of the bathymetry depth in the North Atlantic basin from ECCO.

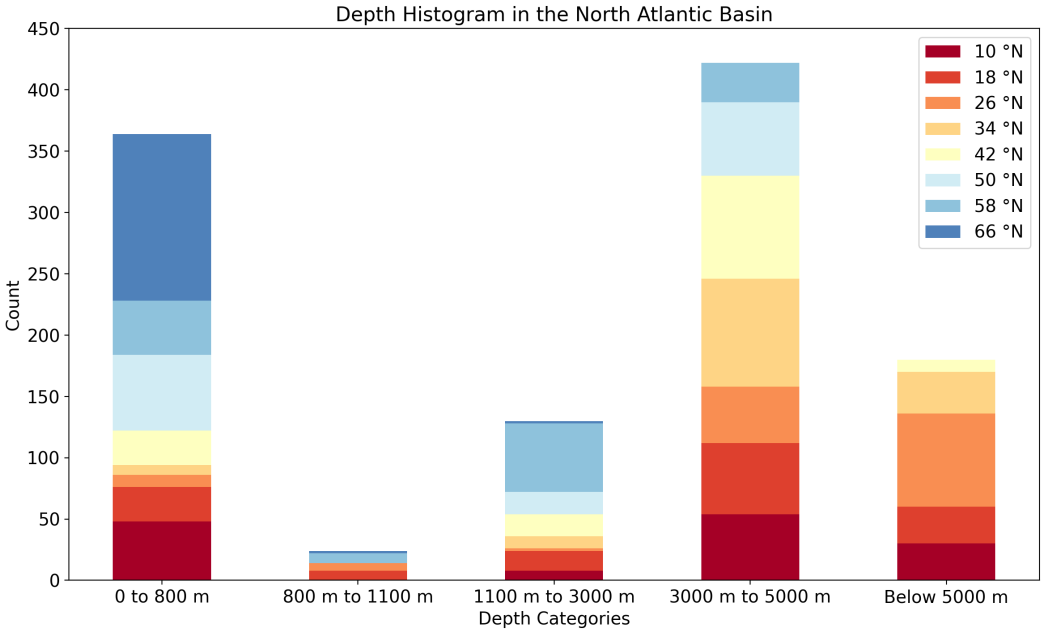


Figure 4.6: Depth Histogram of the North Atlantic basin for specific latitudes from ECCO.

4.2.1 Region of 26 °N

In the initial step, we evaluate the MT anomaly estimation using ECCO OBP data at 26 °N by comparing it with the in-situ MT anomaly estimation performed by RAPID. Figure 4.7 shows the MT anomalies derived from ECCO OBP data (indicated by a light blue line) and from RAPID data (indicated by a light green line) for the region at 26 °N. To obtain a smoother signal, low-pass filtering was applied, with the filtered ECCO OBP data shown as a dark blue line and the filtered RAPID data shown as a green line. The correlation coefficient between the two time series was also calculated. On the left side of Figure 4.7, the MT anomaly time series estimates for both data products for the LNADW at 26 °N, corresponding to the depth layer between '3000 m and 5000 m', are presented. On the right side, the estimates for the ABW at 26 °N are displayed. Table 4.2 summarizes the statistics calculated for Figure 4.7. The results demonstrate that the MT anomaly estimation via ECCO OBP using Equation 3.19 is validated, particularly for the LNADW. For this region, with numerous OBP values distributed along the bathymetry, a correlation coefficient of $R = 0.68$ shows good agreement between the anomaly time series.

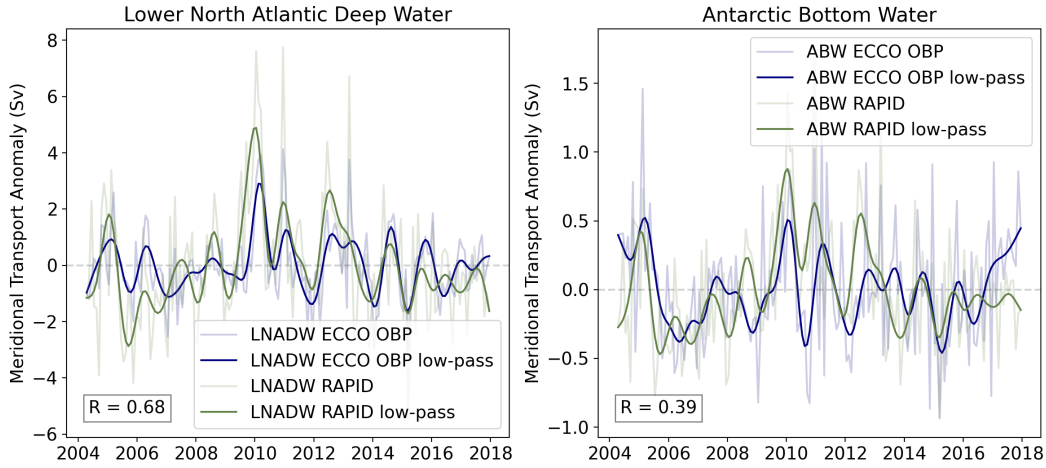


Figure 4.7: Comparison between the meridional transport anomalies from ECCO and RAPID at 26 °N for 2004-02 to 2017-12.

Table 4.2: Standard deviation (σ), root mean square difference (RMS) and correlation coefficient (R) for the layer transport anomalies LNADW and ABW at 26 °N.

Transport Type	Lat.	σ (Sv)	RMS (Sv)	R
LNADW	26 °N	OBP: 1.25, RAPID: 2.1	1.05	0.68
ABW	26 °N	OBP: 0.42, RAPID: 0.42	0.29	0.39

4.2.2 North Atlantic

The MT anomaly estimation with ECCO OBP data using Equation 3.19 was validated through the comparison between model and in-situ data shown in section 4.2.1. This validation allows the analysis to be extended to the entire NA region, where the MT anomaly estimation using ECCO OBP and OVEL data can be compared. The method in Equation 3.19 is thus validated by methodologically comparing it to Equation 3.25 analyzing the MT anomaly estimations for the LNADW and the ABW.

As previously mentioned, the accuracy of the MT estimation using Equation 3.19 heavily depends on the number and distribution of OBP values along the bathymetry. Consequently, the correlation coefficient between the MT estimates from OBP and OVEL data was used to exclude meridional cross sections at specific latitudes with a correlation coefficient below $R = 0.5$. Figure 4.8 shows the MT anomaly estimation for the LNADW from ECCO OBP (light blue line) and OVEL (light red line) for selected latitudes where the correlation coefficient is $R > 0.5$. Low-pass filtering was applied to obtain a smoother signal and reduce intra-annual variability in the MT anomaly estimations from ECCO OBP (dark-blue line) and OVEL data (red line). The correlation coefficient was calculated between both data products for each selected latitude. A similar analysis was conducted for the ABW, as shown in Figure 4.9. The methodology, nomenclature, and analysis are the same as in Figure 4.8. The statistics for the LNADW (Figure 4.8) and the ABW (Figure 4.9) are summarized in Table 4.3.

Table 4.3: Statistics of the layer transport anomalies at various latitudes for ECCO OBP and OVEL estimates in the North Atlantic. The latitude, standard deviation, root mean square difference, and correlation coefficients are presented as Lat., σ, RMS, and R, respectively.

Transport Type	Lat.	σ (Sv)	RMS (Sv)	R
LNADW	12 °N	OBP: 1.04, VEL: 1.85	0.97	0.93
	26 °N	OBP: 1.22, VEL: 1.08	0.44	0.93
	31 °N	OBP: 0.92, VEL: 1.64	0.84	0.93
	37 °N	OBP: 0.94, VEL: 1.64	0.96	0.86
	40 °N	OBP: 0.83, VEL: 0.93	0.50	0.84
	44 °N	OBP: 0.74, VEL: 1.38	1.11	0.59
ABW	13 °N	OBP: 0.15, VEL: 0.05	0.12	0.69
	23 °N	OBP: 0.31, VEL: 0.30	0.19	0.80
	24 °N	OBP: 0.35, VEL: 0.94	0.74	0.71
	26 °N	OBP: 0.43, VEL: 0.85	0.62	0.71
	28 °N	OBP: 0.36, VEL: 0.29	0.16	0.89
	29 °N	OBP: 0.25, VEL: 0.17	0.11	0.93

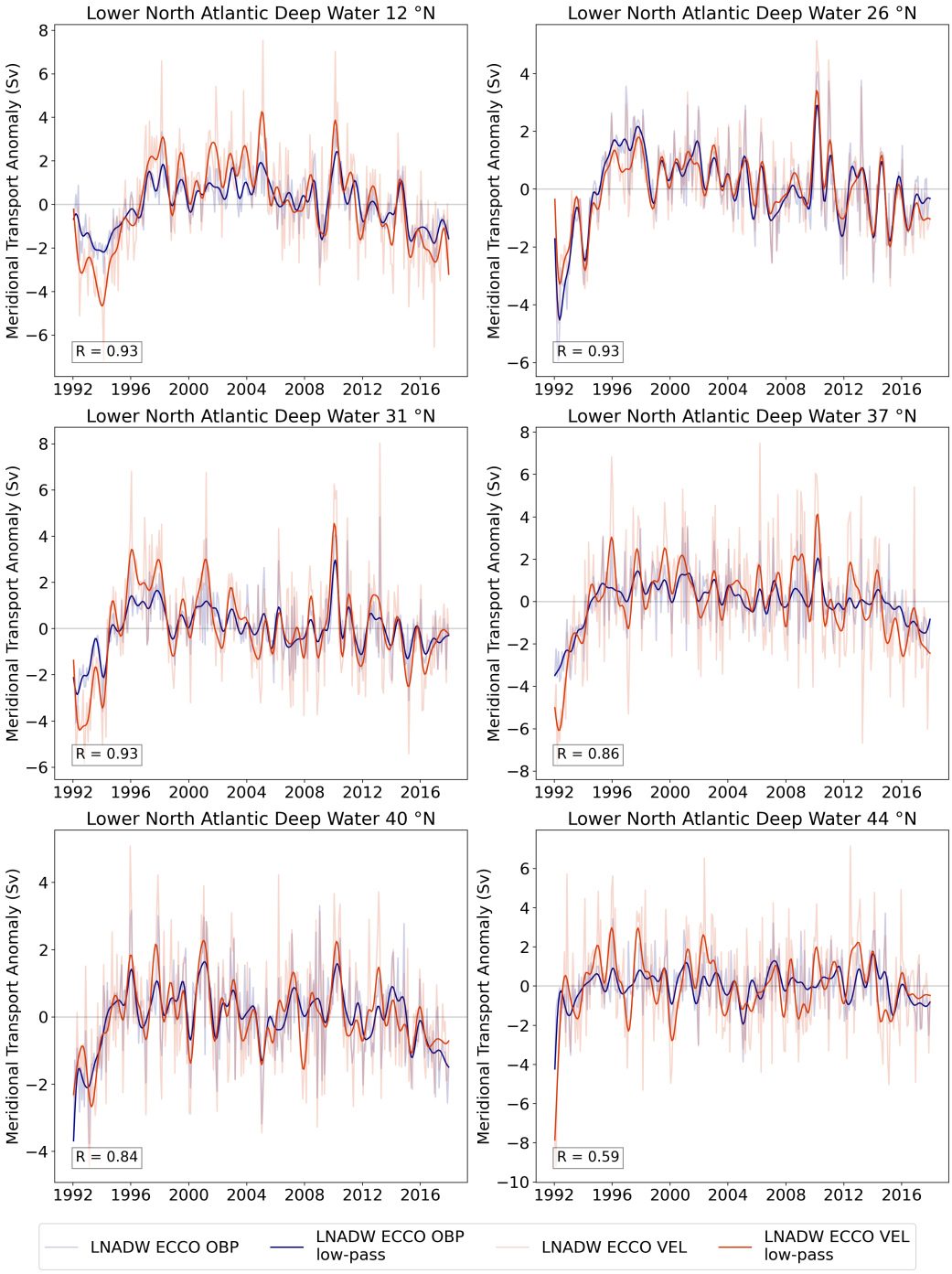


Figure 4.8: Comparison between the Lower North Atlantic Deep Water meridional transport anomalies from ECCO OBP and ECCO VEL at various latitudes in the North Atlantic basin for 1992-01 to 2017-12.

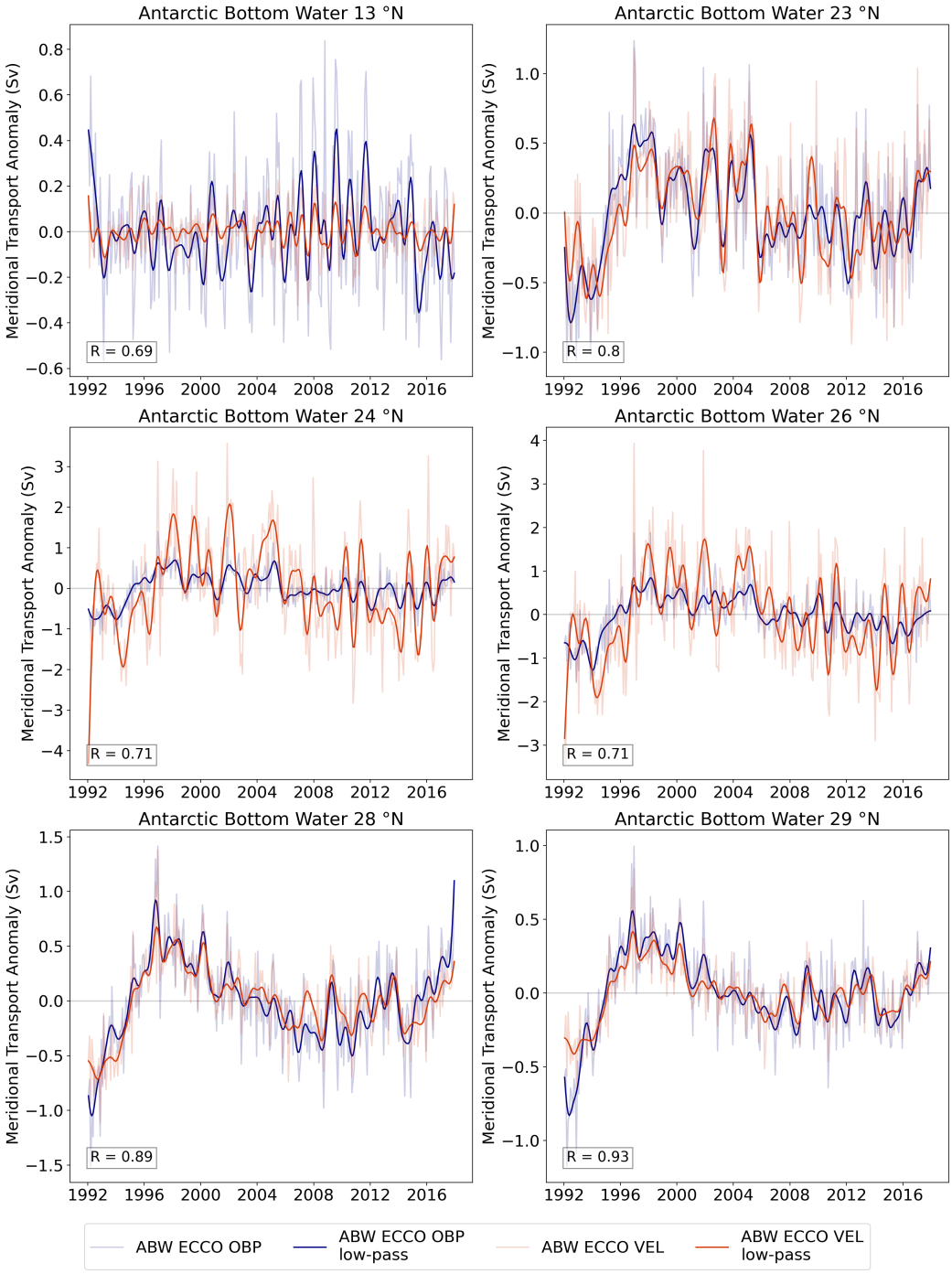


Figure 4.9: Comparison between the Antarctic Bottom Water meridional transport anomalies from ECCO OBP and ECCO VEL at various latitudes in the North Atlantic basin for 1992-01 to 2017-12.

4.3 Meridional Transport Anomaly Estimation from synthetic GRACE/GRACE-FO

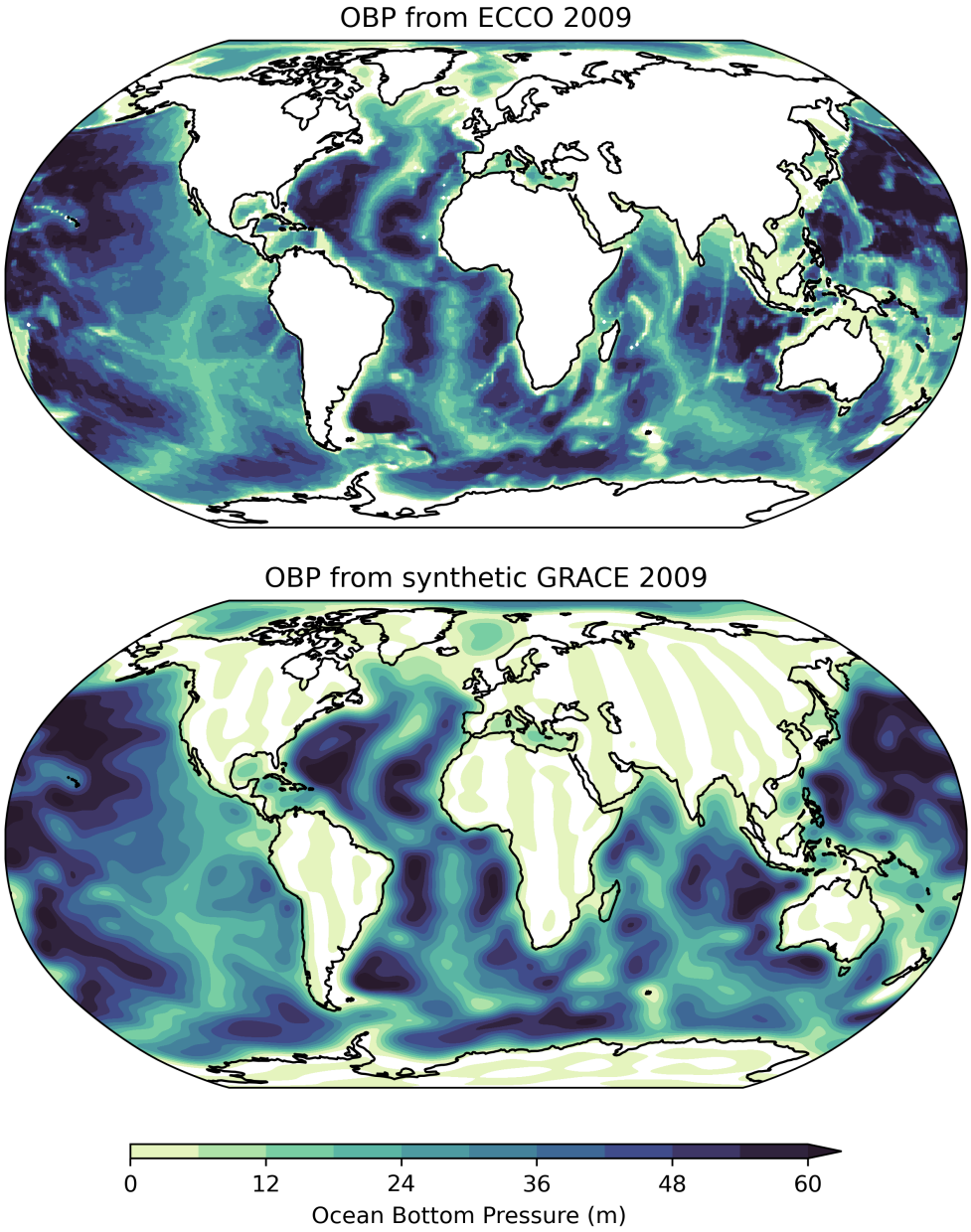


Figure 4.10: Mean OBP for the year 2009, in the top for ECCO data and in the bottom for synthetic GRACE data.

Figure 4.10 illustrates the comparison between the OBP from ECCO and synthetic GRACE/GRACE-FO OBP for the year 2009. The additional noise and subsequent filtering clearly result in a reduction in resolution, similar to what is observed in actual GRACE/GRACE-FO data. The light yellow zonal bands visible on the continents in the synthetic GRACE/GRACE-FO data are artifacts introduced by the synthetic noise, which simulates real GRACE/GRACE-FO noise. These artifacts can

be disregarded as they are located on the continents, their magnitude is insignificant, and our focus is on the NA region shown in section 3.1.

We adhere to the defined latitudes for the LNADW and ABW previously selected for the estimation comparison in Figure 4.8 and Figure 4.9, aiming for an overall comparison between MT estimates from ECCO OBP and synthetic GRACE/GRACE-FO OBP. The data products were initially deseasonalized and detrended, as detailed in section 4.2, resulting in improved estimations. Although the real GRACE/GRACE-FO project started in February 2004, we utilized the entire comparable period from ECCO, spanning from January 1992 to December 2017, to facilitate a comprehensive intercomparison between the two approaches. Figure 4.11 and Figure 4.12 display the MT anomaly estimation for the LNADW and ABW from ECCO OBP (light blue) and synthetic GRACE/GRACE-FO OBP data (light magenta), by using Equation 3.19 for the same latitudes as defined in section 4.2. Low-pass filtering was applied to obtain a smoother signal, reduce intra-annual variability in the MT anomaly estimations from ECCO OBP (dark-blue line), and mitigate the strong noise inherent in the synthetic GRACE/GRACE-FO OBP data (magenta line). The correlation coefficient was calculated between both data products for each selected latitude. Similar analysis were conducted both for the LNADW and ABW. To summarize the statistics for the LNADW and ABW, Table 4.4 was created.

Table 4.4: Statistics of the layer transport anomalies at various latitudes for ECCO and synthetic GRACE/GRACE-FO estimates in the North Atlantic. Latitude, standard deviation, root mean square difference, and correlation coefficients are represented as Lat., σ, RMS, and R, respectively.

Transport Type	Lat.	σ (Sv)	RMS (Sv)	R
LNADW	12 °N	ECCO: 1.04, GRACE: 1.04	1.07	0.47
	26 °N	ECCO: 1.22, GRACE: 0.73	1.33	0.15
	31 °N	ECCO: 0.92, GRACE: 0.76	1.93	0.40
	37 °N	ECCO: 0.94, GRACE: 0.96	0.91	0.54
	40 °N	ECCO: 0.83, GRACE: 0.71	0.69	0.60
	44 °N	ECCO: 0.74, GRACE: 0.39	0.55	0.68
ABW	13 °N	ECCO: 0.15, GRACE: 0.33	0.28	0.51
	23 °N	ECCO: 0.31, GRACE: 0.31	0.37	0.27
	24 °N	ECCO: 0.35, GRACE: 0.33	0.38	0.36
	26 °N	ECCO: 0.43, GRACE: 0.39	0.30	0.72
	28 °N	ECCO: 0.36, GRACE: 0.26	0.28	0.63
	29 °N	ECCO: 0.25, GRACE: 0.18	0.23	0.46

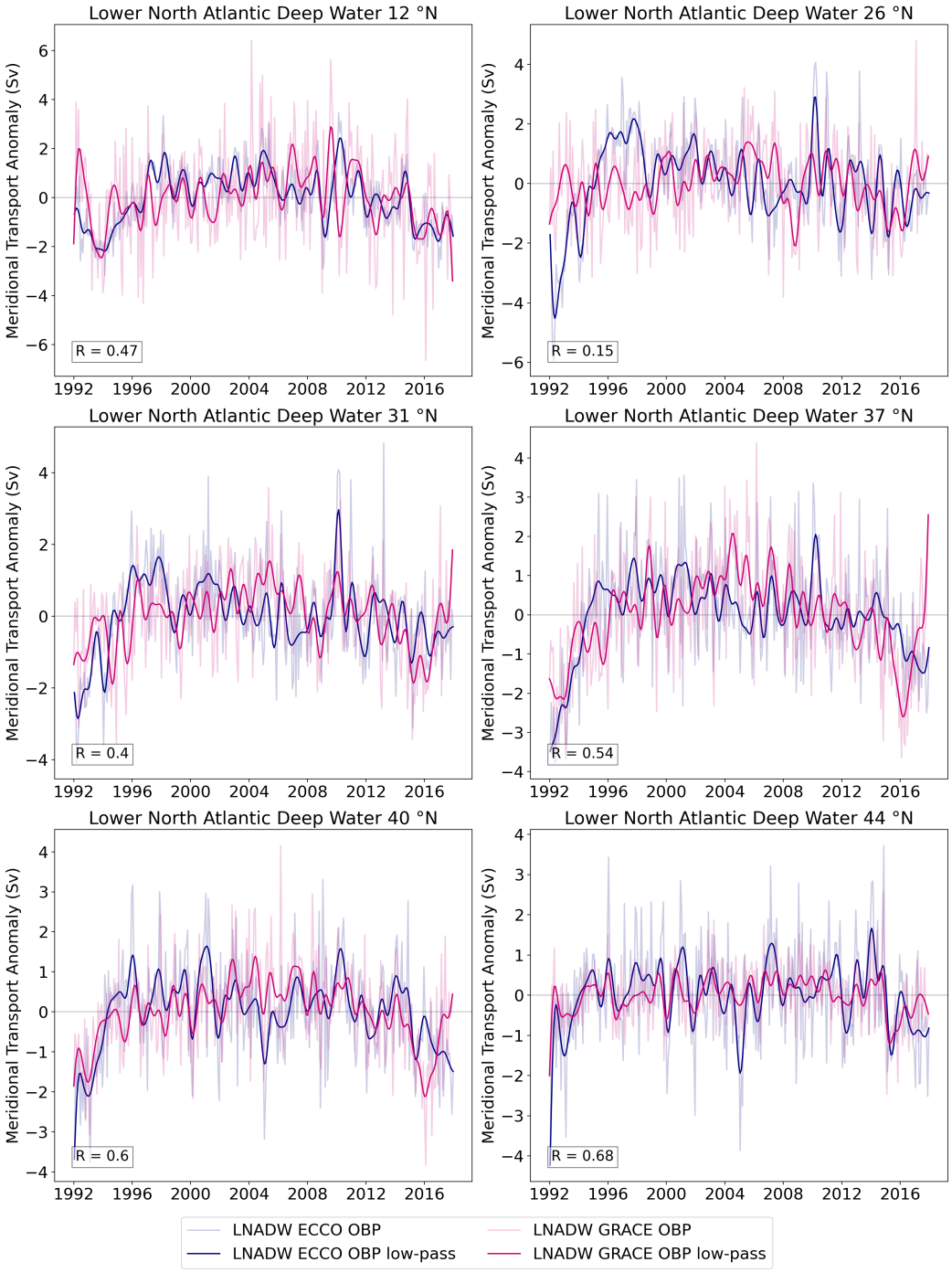


Figure 4.11: Comparison between the Lower North Atlantic Deep Water meridional transport anomalies from ECCO OBP and synthetic GRACE/GRACE-FO OBP at various latitudes in the North Atlantic basin for 1992-01 to 2017-12.

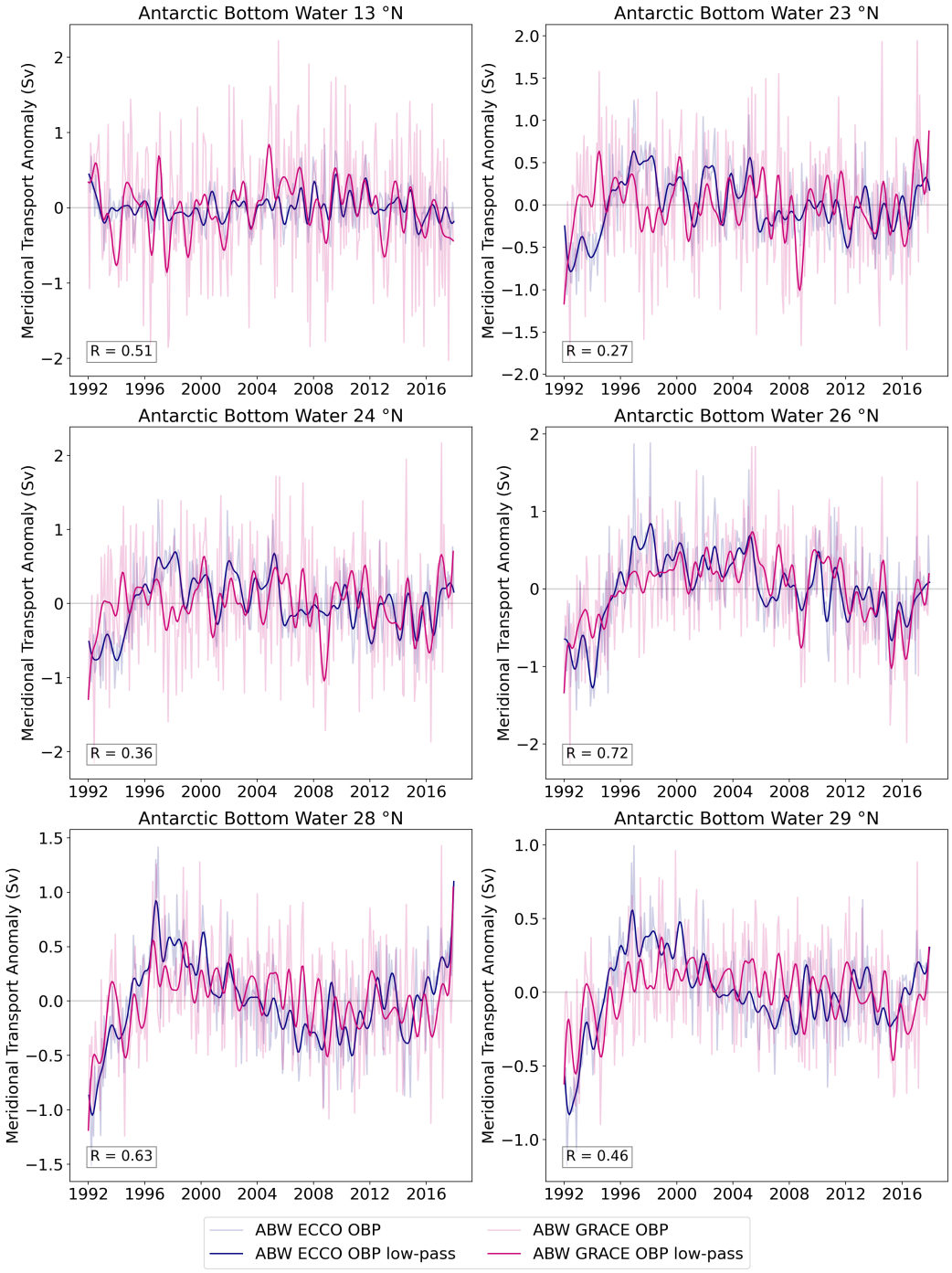


Figure 4.12: Comparison between the Antarctic Bottom Water meridional transport anomalies from ECCO OBP and synthetic GRACE/GRACE-FO OBP at various latitudes in the North Atlantic basin for 1992-01 to 2017-12.

5 Discussion

5.1 Meridional Transport Estimation from RAPID at 26 °N

The MT for the component and layer transports of the AMOC are illustrated in Figure 4.1 and Figure 4.2, respectively. Significant intraannual variability is evident in each component and layer transport, reflecting the pronounced seasonal cycle of the AMOC and its components. This seasonal variation is further emphasized by the climatological monthly means over 2004-04 to 2022-02. The MOC exhibits its highest seasonal MT in late autumn, whereas the upper ocean transports, such as the FS and ET, show their peak seasonal transport values in summer. Conversely, the deep ocean currents, including the LNADW and the ABW, have their peak transport values in the late winter/early spring months. Table 4.1 depicts the statistics of the component and layer transports. The mean state of the MOC is 16.74 Sv for the observational period ranging from April 2004 to February 2022. An abrupt reduction in the mean state of the MOC of around 35 % is visible in Figure 4.1 between 2009 and 2010, affecting every component and layer transport of the AMOC, with the FS as an exception. This abrupt reduction event coincided with cold winters in Europe due to an altered pattern of thermal heat exchange between the ocean and atmosphere over the NA resulting in a reduction in heat transport (Bryden et al., 2014). This abrupt slow-down event is consistent with the literature (Bryden et al., 2014; Landerer et al., 2015; Smeed et al., 2018).

Regarding Table 4.1, all transports, except the LNADW, are directed northward, as positive values correspond to northward and negative values to southward transport. The abrupt slowdown event between 2009 and 2010 is evident in a decrease of the northward transport in the MOC and the ET and a reduction in the southward transport of the LNADW, whereas the overall net northward transport of the ABW experienced an increase. Surprisingly the FS transport seems to be unaffected by this abrupt slowdown. This may be due to the small and narrow passage through which the water traverses. On the other hand, as mentioned before, the northward transport of the deep ABW increased during this event. This result from the capability of the ABW to push further north in an overall reduced state of overturning, as the counteracting force of the southward transport of the LNADW is weakened, as seen

in Figure 4.2. The FS transport has the highest mean MT of all component and layer transports, as the water has to traverse through the narrow passage between Florida and the Bahamas. The wind-driven ET has the smallest mean MT, amounting to 3.74 Sv. The mean MT of the LNADW and the ABW is -5.76 Sv and 1.06 Sv, indicating net southward and northward transport, respectively. As mentioned earlier, the strength of the ABW is heavily dependent on the strength of the LNADW. Positive LNADW anomalies correspond to positive ABW anomalies and vice versa. The weaker the mean state of southward transport by the LNADW, the stronger the northward transport of the ABW, allowing it to penetrate further north, and vice versa. This relationship is underscored by the correlation coefficient between the LNADW and ABW transports, which is nearly a perfect positive correlation of $R = 0.95$. As demonstrated in Figure 4.3, the AMOC exhibits a quasi-closed structure over the entire depth range. Consequently, the northward transport of the upper ocean between 0 m and 1000 m must be compensated by the deep southward return flow between 1000 m and 5000 m. The closure of transport and the near-perfect correlation between the LNADW and ABW suggest that the individual layer transports of the AMOC are interrelated. Therefore, variability in one layer is reflected and has to be observable in all other layers. This interdependence may imply that it is possible to project the entire AMOC and its layer transports by estimating solely the cross-sectional MT of a single layer, e.g. LNADW. This requires further research and may be of interest for future studies.

Additionally, decadal linear trends were calculated for each component and layer transport, as seen in Table 4.1. For the period 2004-04 to 2022-02 MOC is found to decrease at a rate of 1.35 Sv per decade, with a corresponding standard deviation of $1\sigma = \pm 2.32$ Sv. Statistically, this trend is not significant since it lies within one standard deviation. This observation extends to all other component and layer transports listed in Table 4.1. Although the observed seasonality and internal variability exceed the trends estimated from linear regression, the decadal trends of the individual component and layer transports warrant concern. Even though the observational period spans 20 years only, this demonstrates that the AMOC has been in a phase of reduced overturning in recent years, consistent with the literature (Bryden et al., 2014; Smeed et al., 2018; Westen et al., 2024). The FS transport is also decreasing, though at a smaller magnitude of 0.42 Sv/decade. Surprisingly, the ET has increased by 0.29 Sv/decade in recent years, probably induced by changes in wind patterns due to climate change. As mentioned previously, the LNADW and ABW are strongly correlated. The net southward flow of the LNADW is decreasing by 0.95 Sv/decade, which allows the net northward transport of the ABW to increase by 0.22 Sv/decade. This represents a decrease of the LNADW and an increase of the ABW by 16.5 % and 20.0 % per decade with respect to the mean state, respectively.

The detailed analysis of the stream function and the DMO provides insights into the vertical and temporal dynamics of the AMOC, as seen in Figure 4.3. The prominent slowdown of the AMOC is also apparent in the stream function, indicated by a vertical blue contour traversing through depth direction in the period between 2009 and 2010. Additionally, further slowdowns of the AMOC are visible in the stream function, as seen in the years 2005, 2013, and 2018, again indicated by vertical blue contours traversing through depth direction. As aforementioned, the AMOC exhibits a closed vertical transport structure, evidenced by the near-zero net transport at the maximum depth of the streamfunction. However, disturbances can arise from net zonal mass transport variations, originating from sources such as the Bering Strait inflow and net freshwater input from the Greenlandic Ice Sheet meltwater. According to Landerer et al. (2015), these disturbances are negligible compared to the overall net transport. The mean DMO (Figure 4.3 left) over the entire observational period is estimated at 1017.6 m. The DMO also implies intraannual variability, resulting from the overall variability of the MOC, which depends on the strength of the net northward transport. The slow-down event between 2009 and 2010 is also evident in the DMO, although it appears to lag behind the initial disturbance signal. As a consequence of this slow-down event, the DMO shifts to shallower levels, with a notable peak observed around 2011.

In-situ measurements like RAPID provide an indispensable source of observational, real-time data for the MT at a specific latitude. Nevertheless, arrays such as RAPID, Overturning in the Subpolar North Atlantic Program (OSNAP), and South Atlantic Meridional Overturning Circulation Basin-wide Array (SAMBA) are confined to certain latitudes or regions, limiting their spatial coverage. Despite this limitation, these arrays are crucial for estimating the absolute state of the AMOC and within the framework of this study.

5.2 Validation of Meridional Transport Anomaly Estimations from ECCO

Constrained by the latitudinal dependence of in-situ AMOC hydrographic estimates, such as those from RAPID, it is imperative to continuously monitor AMOC variability across both spatial and temporal dimensions. Consequently, the analysis was extended to encompass the entire NA region. For the validation of the MT estimations from ECCO OBP data using Equation 3.19, the region, spanning from 10 °W to 80 °W and 10 °N to 66.5 °N, was selected. The equatorial region was excluded because the geostrophic assumption, which forms the basis for Equation 3.19, breaks down there due to the vanishing Coriolis force. The MT estimation from ECCO OBP data is highly dependent on the distribution of OBP values across the cross-sectional

bathymetry given in the dataset. Consequently, the cross-sectional bathymetry of this region was analyzed in equal steps, as shown in Figure 4.4. The bathymetry becomes shallower towards the north, particularly at high latitudes due to the presence of the continental shelf of Greenland (Figure 4.5). As previously mentioned, the quality of the MT estimation by OBP is mainly dependent on the distribution of OBP values across the cross-sectional bathymetry. Figure 4.6 presents the depth/OBP value distribution for pre-selected latitudes.

To recap, each depth value of the ocean bathymetry given a zonal cross-section in the ECCO dataset grid, corresponds to one unique OBP value. Hence, the distribution of depth values equates to the distribution of OBP values along a cross-sectional bathymetry. The upper layer '0 to 800 m' and deeper layers, such as '3000 m to 5000 m' and 'below 5000 m', contain most of the values distributed along their bathymetries. The uppermost layer '0 to 800 m' was excluded from the analysis due to the steepness of the bathymetric flanks, which leads to a disproportionate relationship between depth increase and the distributed grid points, thereby distorting depth-grid point resolution. The layers '3000 m to 5000 m' and 'below 5000 m', corresponding to the LNADW and ABW respectively, were selected for further analysis due to their significant number of OBP values distributed along their bathymetries and the moderate steepness of the bathymetric slopes.

Initially, the region at 26 °N was analyzed to validate the MT anomaly estimations from ECCO OBP using Equation 3.19 against those estimated from the RAPID array (Figure 4.7) based on deseasonalized and detrended anomalies. For the LNADW at 26 °N, the two signals appear very similar, which is reflected in the root mean square difference of RMS $= 1.05$. The standard deviations for the MT estimations by ECCO OBP and RAPID are $\sigma_{\text{ECCO}} = 1.25$ and $\sigma_{\text{RAPID}} = 2.1$, as shown in Table 4.1. The RMS between the MT from ECCO OBP and RAPID being smaller than the standard deviation suggests that the signals are quite similar. This is further supported by the correlation coefficient between the two time series, which is $R = 0.68$. Similarly, the analysis for the ABW, shown on the right of Figure 4.7, indicates that the RMS is again smaller than the standard deviations of both signals, suggesting similarity. However, the correlation coefficient for the ABW between both signals is lower, $R = 0.39$.

These correlations result from the quality of MT estimation, due to the high number of OBP values distributed along the zonal cross-sections of the LNADW and ABW layers. Furthermore, the depth increase due to steepness in proportion to the grid point distribution on the bathymetry is an additional factor influencing the quality of the MT estimate. The slowdown event of the AMOC between 2009 and 2010 is also evident in the MT estimations from ECCO OBP (Figure 4.7). Both the LNADW and the ABW exhibit a positive anomaly, corresponding to reduced southward transport of the LNADW and an enhancement of the strength and northward penetration of

the ABW. Again, it is evident that the variability in one layer is mirrored in the other, as demonstrated by the correlation coefficient between the MT anomaly estimates from OBP for the LNADW and ABW at 26°N, which is $R = 0.52$. Although the magnitude of the correlation is smaller as in comparison to the RAPID estimates, it remains significant. Furthermore, it is important to consider that geostrophic estimates neglect friction with the ocean bathymetry, which is particularly significant for the ABW due to its transport being in contact with the ocean floor. This neglect of friction may result in the reduction of correlation between both signals.

Hence, given a zonal cross-section in the NA basin and depth layer at latitude ϕ, the MT of ocean water perpendicular through this cross-section can be estimated solely using Equation 3.19 by integrating the product of OBP and the ocean bathymetry slope along the zonal extent of the corresponding bathymetry. This estimation was verified and validated through comparison with the in-situ RAPID data.

Verification with in-situ data allowed for the expansion of the analysis to the whole region of the NA. In section 4.2.2, the MT estimation from ECCO OBP data by Equation 3.19 was verified with MT estimated from ECCO OVEL data by Equation 3.25, providing a methodological validation. The LNADW water (seen in Figure 4.8) and the ABW (seen in Figure 4.9) were analyzed. Depth-grid point resolutions and the number of OBP values distributed along the cross-sectional bathymetry were the determining factors of the quality of MT estimation by ECCO OBP data. Due to the fact that some cross-sections and bathymetry flanks do not possess these two features in appropriate quality, those latitudes were chosen where the correlation coefficient of the signals of the MT estimation between OBP and OVEL data exceeded $R = 0.5$. All estimations show very similar anomaly signals. The RMS of all estimations appears to be smaller or within the range of $\pm 1.5\,\sigma$ (Table 4.3), which indicates that the signals are quite similar. The estimated magnitudes of the LNADW and ABW are obviously dependent on latitude, thereby providing clear evidence that the magnitude of variability is influenced by latitude. The only estimations where the similarity between the two signals is given but the magnitude of the two signals differ are the estimations for the ABW at 13 °N, 24 °N, and 26 °N. The reason for this is the smaller number of OBP values distributed along these cross-sectional bathymetries compared to others, leading to a smaller magnitude of the signal, hence influencing the quality of the estimations.

The encouraging quality of the estimations in the NA region for the LNADW and ABW at specific latitudes is underscored by the correlation coefficients also provided in Table 4.3. The transport signals also seem to propagate along latitude, meaning that the transport at a specific latitude is correlated to the transport at another latitude further north or south. Especially strong signals, such as the abrupt slow-down event between 2009 and 2010, can be seen at all latitudes of the LNADW, except in the estimate for 44 °N. A plausible explanation for this is that changes in the AMOC

exhibit latitudinal dependence and are specific to gyres (Subtropical or Subpolar). Consequently, variability may manifest differently north and south of 40 °N (Landerer et al., 2015), especially for the LNADW. In contrast, these distinct signal characteristics are not observed in the ABW, as it does not extend much beyond 30 °N. This is evident in Figure 4.9, which shows no transport anomalies for the ABW beyond 29 °N. As previously discussed in section 2.2, the region indicating the boundary between the Subtropical and Subpolar Gyre (around 40 °N) acts as a pacemaker for decadal AMOC variability, with these decadal changes propagating meridionally from this region (Buckley and Marshall, 2016). According to Bingham and Hughes (2009), low-frequency modes (i.e., decadal variability) are more pronounced north of this transition zone compared to regions further south. This is due to the weak stratification in the NA Subpolar Gyre, which impedes the free propagation of waves. Consequently, this boundary or transition zone is crucial for future AMOC variability analysis, as it dictates the pace and structure of variability within the overturning system.

To conclude, given a zonal cross-section in the NA basin with sufficient depth-to-grid point resolution and a sufficient number of OBP values distributed along the bathymetry, the MT perpendicular to this cross-section can be estimated using solely Equation 3.19. This estimation was validated with in-situ data from RAPID and methodologically verified using OVEL data from ECCO, as shown in Equation 3.25. Additionally, transport signals propagate meridionally. Hence, an alteration of the MT of a specific layer at a specific latitude is also visible at other layers and latitudes. In terms of the propagation of variability signals, the boundary region between the Subtropical and Subpolar Gyre act as a margin. The signals exhibit different characteristics north and south of this boundary region. Furthermore, the quasi-closed structure results in the interconnection between layer transports, causing the variability of one layer to be mirrored in the other, as seen in the LNADW and ABW. All of this emphasizes the interplay and connection between all the individual component and layer transports of the AMOC, leading to the opportunity for future research to estimate the entire Atlantic Meridional Overturning Circulation by solely observing and estimating one specific layer, such as the LNADW.

5.3 Meridional Transport Anomaly Estimation from synthetic GRACE/GRACE-FO

The creation of the synthetic GRACE/GRACE-FO data set, as outlined in section 3.6.1, is visualized for OBP data from the year 2009 in Figure 4.10. This process results in a reduced resolution analogous to that observed in the actual GRACE/GRACE-FO project, thereby highlighting the intrinsic challenges of GRACE/GRACE-FO data:

substantial noise and limited resolution. The noise level in GRACE/GRACE-FO data is significantly surpassing the underlying signal in magnitude, complicating the discrimination between the two.

The MT anomaly estimates derived from ECCO and synthetic GRACE/GRACE-FO OBP data, utilizing Equation 3.19, are demonstrated in Figure 4.11 and Figure 4.12 for the LNADW and ABW, respectively. Although the root mean square (RMS) difference between the signals remains within or below $1.5\,\sigma$ as reported in Table 4.4, suggesting substantial similarity, some of the correlation coefficients also listed in Table 4.4 fall below the critical threshold of $R = 0.5$. Specific regions within the LNADW and ABW basins exhibit correlation coefficients beneath this threshold, with the ABW providing more reliable estimates overall. The inevitable spatial filtering to substantially reduce noise in the MT estimates from synthetic GRACE/GRACE-FO data leads to significant information loss regarding the main signal, indicating a trade-off between noise reduction and retention of the original signal. Additionally, the dependency of MT estimates on the bathymetry's slope steepness is impeded by the coarse resolution of GRACE/GRACE-FO (about 300 km) compared to the finer resolution of ECCO model data, hence not capturing the full available information on the slopes. This effect is particularly pronounced in regions with steep bathymetries, such as the 26 °N cross-section within the LNADW layer. In contrast, GRACE/GRACE-FO captures signal variability more effectively in bathymetric cross-sections with sufficient horizontal extent, as illustrated in Figure 4.4. These improved estimates in the ABW result from the corresponding bathymetry representing the ocean floor, hence providing a sufficient horizontal extent to be captured by GRACE/GRACE-FO.

We are using monthly OBP grids, meaning for GRACE/GRACE-FO a reduction in spatial resolution. The inherent trade-off between temporal and spatial resolution in GRACE/GRACE-FO data, could be optimized by extending the temporal resolution from monthly to annual or longer periods, thereby enhancing MT estimations along steep bathymetric flanks, by means of increasing the spatial resolution. Despite these limitations, the synthetic GRACE/GRACE-FO data yield promising MT estimates in regions with moderate bathymetry steepness and adequate horizontal extension, as evidenced by the estimates of the LNADW at 44 °N and the ABW at 26 °N, with correlation coefficients of $R = 0.68$ and $R = 0.72$, respectively. These results underscore the potential benefits of advancing spatial resolution in remote-sensing systems like GRACE/GRACE-FO.

One promising upcoming candidate in remote-sensing is the Masschange and Geosciences International Constellation (MAGIC) project (Haagmans and Tsaoussi, 2020). MAGIC observes mass anomalies by measuring changes in the time-dependent gravity field, similar to GRACE/GRACE-FO. Unlike GRACE/GRACE-FO, MAGIC features two in-line formation flying and inclined satellite pairs, with the satellites flying only 100 km apart (compared to 220 km for GRACE/GRACE-FO (Adam, 2002)),

with one pair in a polar orbit and the other in an inclined one of 67 ° (Haagmans and Tsaoussi, 2020). This arrangement doubles the space-time sampling and significantly improves the East-to-West sensitivity (Haagmans and Tsaoussi, 2020). However, fast mass changes in the atmosphere and oceans remain the largest error sources for time-variable gravity models (Haagmans and Tsaoussi, 2020). The noise in MAGIC data is expected to be 5 to 10 times smaller than in GRACE/GRACE-FO data (Haagmans and Tsaoussi, 2020), addressing the need for strong spatial filtering that currently leads to a loss of information in the underlying signal. The MAGIC double pair configuration improves the OBP East-to-West information content in the ocean basin, on which the integral in Equation 3.19 is dependent on. Moreover, MAGIC will enable solely satellite-based solutions given on daily to weekly timescales, which is impossible with the latest generation of gravity missions (Haagmans and Tsaoussi, 2020). Consequently, even weekly to intra-annual AMOC variations may be observable with appropriate quality in the future.

To summarize, GRACE/GRACE-FO can capture MT anomalies for certain bathymetric cross-sections and layers with the constraint of having sufficiently gentle bathymetries and horizontal extent. A trade-off between spatial and temporal resolution is necessary to assure the quality of the estimation. Upcoming projects like MAGIC will enhance both temporal and spatial resolutions, reduce latency, decrease the significance of post-processing, improve East-to-West sensitivity, and provide new monthly and/or sub-monthly gravity fields, therefore being an encouraging perspective in terms of AMOC monitoring. This will inevitably improve the MT estimations derived solely from satellite gravimetry data by Equation 3.19.

6 Conclusion and Outlook

In this thesis, the underlying principles and driving mechanisms of the AMOC were thoroughly investigated. Each component and layer of the AMOC exhibited pronounced seasonality and short-term variability. Analysis of RAPID data revealed that the AMOC is in a phase of reduced overturning, highlighted by a declining trend of the MOC of -1.35 Sv/decade with a corresponding standard deviation of $\pm$ 2.32 Sv. Even though the trend is not significant due to pronounced seasonality and intraannual variability, a decrease seems to emerge. Decreasing transport of the LNADW and increasing transport of the ABW indicate interconnectivity between layers, supported by a high correlation coefficient of $R = 0.95$ between the two signals, derived from in-situ data. Noteworthy events, such as the AMOC slowdown between 2009 and 2010, were observed in all layers except the FS transport, likely due to the narrow passage the water has to traverse through in this region. Additionally, an analysis of the stream function over the entire available period demonstrated that the AMOC forms a quasi-closed structure, where northward transport of upper ocean currents (0 to 1000 m) is compensated by southward transport of deep ocean currents (1000 m to 5000 m). Significant events like the 2009 to 2010 slowdown were also evident in the stream function. The mean depth of maximum overturning was estimated to be 1017.6 m.

It was demonstrated that the complex in-depth integration mechanism for MT along a zonal cross-section at latitude ϕ, as utilized in previous studies (Kanzow et al., 2009; Bingham and Hughes, 2009; Landerer et al., 2015), can be replaced by a simplified integration mechanism of OBP values along the longitudinal cross-sectional basin extent. This new approach eliminates the need to account for intervening topography, such as the MAR, required in previous methodologies. This MT anomaly estimation approach with ECCO OBP data was validated using MT anomalies from the RAPID array at 26 °N, resulting in correlation coefficients of 0.68 and 0.39 for the LNADW and ABW, respectively, similar to estimates from (Landerer et al., 2015). A methodological validation of the MT anomaly estimation by Equation 3.19 was conducted for the entire NA region by comparing it to MT anomaly estimates derived from OVEL using Equation 3.25. Encouraging similarities were observed. Notably, the correlation coefficient between MT anomaly estimates from OBP and OVEL data at 26 °N, corresponding to the RAPID location, has been estimated to $R = 0.93$ for the LNADW. The quality of the MT estimation was primarily determined by the number of OBP values distributed along the cross-section bathymetry and the

depth-to-value distribution gradient (i.e. bathymetry steepness). Distinct signal characteristics were identified north and south of 40 °N, marking the boundary between the Subtropical and Subpolar Gyre, due to the different stratification properties of the gyres. Anomalies estimated from ECCO OBP for the LNADW were also reflected in ABW anomalies, although with a lower correlation coefficient of $R = 0.52$ for ECCO estimates. This may result from the neglect of frictional effects with the ocean bathymetry in geostrophic calculations as used in this approach.

In the final part of this thesis, the capability of GRACE/GRACE-FO to capture AMOC variability was analyzed. This analysis involved creating synthetic GRACE/GRACE-FO OBP data, estimating cross-sectional MT anomalies, and comparing these to MT anomaly estimates derived from ECCO OBP. The inherent limitations of GRACE/GRACE-FO, namely the spatial-temporal trade-off in resolution, the overall coarse spatial resolution, and the superimposed noise that exceeds the underlying signal by several magnitudes, restrict the accuracy of MT anomaly estimations by GRACE/GRACE-FO. These limitations reduce the capability of capturing the signal at steep flanks, further impacting the precision of the estimate. Nevertheless, it was demonstrated that for certain layers in zonal cross-sections with sufficiently gentle bathymetry and adequate horizontal extent, GRACE/GRACE-FO is capable of monitoring monthly AMOC variability. In particular, the ABW, with its bathymetry corresponding to the ocean floor and therefore resulting in a very large horizontal extent, is best suited for this purpose and showed overall encouraging results. Upcoming remote-sensing missions like MAGIC will significantly enhance the ability to monitor AMOC variability, even on weekly to intra-annual time scales. By providing signals with reduced superimposed noise, higher spatial resolution, and higher East-to-West sensitivity, upcoming missions like MAGIC will further improve cross-sectional MT anomaly estimates derived solely from remote-sensing data by utilizing OBP anomalies in combination with Equation 3.19.

To conclude, given a zonal cross-section at latitude ϕ in the NA basin with sufficient depth-to-grid point resolution and an adequate number of OBP values distributed along the bathymetry, MT perpendicular through this cross-section can be estimated using solely Equation 3.19. This presents a unique opportunity for future research to estimate MT using ECCO model, GRACE/GRACE-FO or MAGIC data for any latitudinal cross-section in any ocean basin and desired depth layer. Other arrays, such as OSNAP positioned in the Subpolar NA or SAMBA located at 34.5 °S, can also be considered as references in future studies. The quasi-closed vertical structure of the AMOC allows for further analyses to estimate the entire AMOC by focusing on a single layer, such as the LNADW or ABW, as variability in one layer is mirrored in others. Future remote-sensing missions will enhance spatial resolution and reduce the signal-to-noise ratio, thereby adding value to MT estimates. In-situ-, model-, and remote-sensing data collectively provide a unique dataset for estimating the mean

state, variability, and evolution of the AMOC, and extending these analyses to other ocean basins and currents globally. Monitoring the variability of the AMOC gives us the potential to monitor a changing European climate.

List of Tables

3.1 Variables in *moc_transports* RAPID data. 29

4.1 Mean, linear trend (Lin. Trd.) and standard deviation (σ) of RAPID component and layer transports at 26 °N. 36
4.2 Standard deviation (σ), root mean square difference (RMS) and correlation coefficient (R) for the layer transport anomalies LNADW and ABW at 26 °N. 44
4.3 Statistics of the layer transport anomalies at various latitudes for ECCO OBP and OVEL estimates in the North Atlantic. The latitude, standard deviation, root mean square difference, and correlation coefficients are presented as Lat., σ, RMS, and R, respectively. 45
4.4 Statistics of the layer transport anomalies at various latitudes for ECCO and synthetic GRACE/GRACE-FO estimates in the North Atlantic. Latitude, standard deviation, root mean square difference, and correlation coefficients are represented as Lat., σ, RMS, and R, respectively. 49

List of Figures

2.1 AMOC schematic 6
2.2 Thermocline 7
2.3 Ekman Spiral 7
2.4 Wind Transport 8
2.5 Sea Surface Temperature ECCO 2017 10
2.6 Sea Surface Salinity ECCO 2017 11
2.7 Idealized narrow basin model 12
2.8 AMOC tipping 14

3.1 Global Bathymetry and NA boundaries 18
3.2 North Atlantic Bathymetry 18
3.3 North Atlantic Bathymetry 3D 19
3.4 Plain region A and boundary C at 26 °N 22

3.5 Horizontal components L and Bathymetry B at 26 °N 23
3.6 RAPID location 27
3.7 Atlantic Basin 26 °N cross section 28
3.8 ECCO logo 30
3.9 GRACE-FO assembly and concept 33

4.1 Component transports from RAPID 38
4.2 Component transports from RAPID 39
4.3 Streamfunction (left) DMO (right) from RAPID 39
4.4 Bathymetries North Atlantic 42
4.5 Mean Bathymetry North Atlantic 43
4.6 Depth Histogram North Alantic 43
4.7 Comparison Meridional Transport Anomalies ECCO OBP and RAPID at 26 °N 44
4.8 Comparison LNADW Meridional Transport Anomalies ECCO OBP and ECCO VEL 46
4.9 Comparison ABW Meridional Transport Anomalies ECCO OBP and ECCO VEL 47
4.10 Comparison ECCO and GRACE OBP 48
4.11 Comparison LNADW Meridional Transport Anomalies ECCO OBP and synthetic GRACE/GRACE-FO OBP 50
4.12 Comparison ABW Meridional Transport Anomalies ECCO OBP and GRACE/GRACE-FO OBP 51

Bibliography

Abraham, John P, M Baringer, NL Bindoff, et al. (2013). „A review of global ocean temperature observations: Implications for ocean heat content estimates and climate change“. In: *Reviews of Geophysics* 51.3, pp. 450–483. DOI: 10.1002/rog.20022 (cit. on pp. 2, 12).

Adam, David (2002). „Gravity measurement: Amazing grace.“ In: *Nature* 416.6876, pp. 10–12. DOI: 10.1038/416010a (cit. on pp. 32, 59).

Arrigo, Kevin R, Gert van Dijken, and Matthew Long (2008). „Coastal Southern Ocean: A strong anthropogenic CO2 sink“. In: *Geophysical Research Letters* 35.21. DOI: 10.1029/2008GL035624 (cit. on p. 12).

Bingham, Rory J and Chris W Hughes (2009). „Geostrophic dynamics of meridional transport variability in the subpolar North Atlantic“. In: *Journal of Geophysical Research: Oceans* 114.C12. DOI: 10.1029/2009JC005492 (cit. on pp. 3, 9, 11, 17, 20, 58, 61).

Bryden, HL, Brian A King, Gerard D McCarthy, and EL McDonagh (2014). „Impact of a 30% reduction in Atlantic meridional overturning during 2009–2010“. In: *Ocean Science* 10.4, pp. 683–691. DOI: 10.5194/os-10-683-2014 (cit. on pp. 1, 6, 14, 53, 54).

Buckley, Martha W and John Marshall (2016). „Observations, inferences, and mechanisms of the Atlantic Meridional Overturning Circulation: A review“. In: *Reviews of Geophysics* 54.1, pp. 5–63. DOI: 10.1002/2015RG000493 (cit. on pp. 1, 5–7, 9–13, 27, 28, 58).

Caesar, Levke, Stefan Rahmstorf, Alexander Robinson, Georg Feulner, and V Saba (2018). „Observed fingerprint of a weakening Atlantic Ocean overturning circulation“. In: *Nature* 556.7700, pp. 191–196. DOI: 10.1038/s41586-018-0006-5 (cit. on pp. 6, 14).

Cessi, Paola and C Spencer Jones (2017). „Warm-route versus cold-route interbasin exchange in the meridional overturning circulation“. In: *Journal of Physical Oceanography* 47.8, pp. 1981–1997. DOI: 10.1175/JPO-D-16-0249.1 (cit. on pp. 10–12).

Cheng, Lijing, Karina von Schuckmann, Audrey Minière, et al. (2024). „Ocean heat content in 2023“. In: *Nature Reviews Earth & Environment*, pp. 1–3. DOI: 10.1038/s43017-024-00539-9 (cit. on p. 13).

Demtröder, Wolfgang (2021). *Experimentalphysik 1: Mechanik und Wärme*. ger. 9. Aufl. 2021. Springer-Lehrbuch. Berlin, Heidelberg: Springer Berlin Heidelberg (cit. on p. 9).

ECCO-Consortium, I. Fukumori, O. Wang, et al. (2021a). *ECCO Ocean Bottom Pressure - Monthly Mean 0.5 Degree (Version 4 Release 4b)*. DOI: 10.5067/ECG5M-OBP4B (cit. on pp. 31, 32).

ECCO-Consortium, Ichiro Fukumori, Ou Wang, et al. (Feb. 2021b). *Synopsis of the ECCO Central Production Global Ocean and Sea-Ice State Estimate, Version 4 Release 4*. Version 4 Release 4. DOI: 10.5281/zenodo.4533349 (cit. on pp. 30, 31).

ECCO-group (2024). *ECCO logo*. URL: https://www.ecco-group.org/ (visited on May 4, 2024) (cit. on p. 30).

Fenty, Ian and Ou Wang (2020). *ECCO Ocean Velocity - Monthly Mean 0.5 Degree (Version 4 release 4)*. DOI: 10.5067/ECG5M-OVE44 (cit. on p. 31).

Forget, G., J.-M. Campin, P. Heimbach, et al. (2015). „ECCO version 4: an integrated framework for non-linear inverse modeling and global ocean state estimation“. In: *Geoscientific Model Development* 8.10, pp. 3071–3104. DOI: 10.5194/gmd-8-3071-2015 (cit. on pp. 30, 31).

Frajka-Williams, Eleanor (2015). „Estimating the Atlantic overturning at 26 N using satellite altimetry and cable measurements“. In: *Geophysical Research Letters* 42.9, pp. 3458–3464. DOI: 10.1002/2015GL063220 (cit. on pp. 1, 5, 6, 17, 26).

Garcia-Soto, C., L. Cheng, L. Caesar, et al. (2021). „An Overview of Ocean Climate Change Indicators: Sea Surface Temperature, Ocean Heat Content, Ocean pH, Dissolved Oxygen Concentration, Arctic Sea Ice Extent, Thickness and Volume, Sea Level and Strength of the AMOC (Atlantic Meridional Overturning Circulation)“. English. In: *Frontiers in Marine Science* 8. Cited By :9. DOI: 10.3389/fmars.2021.642372 (cit. on p. 13).

Haagmans, R and L Tsaoussi (2020). „Next Generation Gravity Mission as a Mass-change And Geosciences International Constellation (MAGIC) Mission Requirements Document“. In: *Earth and Mission Science Division, European Space Agency* (cit. on pp. 59, 60).

Holton, James R. and Gregory J. Hakim (2013). *An Introduction to Dynamic Meteorology*. 5th ed. Academic Press (cit. on p. 21).

Ivchenko, VO, Dmitry Sidorenko, Sergey Danilov, Martin Losch, and Jens Schröter (2011). „Can sea surface height be used to estimate oceanic transport variability?“ In: *Geophysical research letters* 38.11. DOI: 10.1029/2011GL047387 (cit. on p. 7).

Johnson, Helen L, Paola Cessi, David P Marshall, Fabian Schloesser, and Michael A Spall (2019). „Recent contributions of theory to our understanding of the Atlantic meridional overturning circulation“. In: *Journal of Geophysical Research: Oceans* 124.8, pp. 5376–5399. DOI: 10.1029/2019JC015330 (cit. on pp. 10–13).

Kanzow, Torsten, HL Johnson, DP Marshall, et al. (2009). „Basinwide integrated volume transports in an eddy-filled ocean“. In: *Journal of Physical Oceanography* 39.12, pp. 3091–3110. DOI: 10.1175/2009JPO4185.1 (cit. on pp. 20, 61).

Kornfeld, Richard P, Bradford W Arnold, Michael A Gross, et al. (2019). „GRACE-FO: the gravity recovery and climate experiment follow-on mission“. In: *Journal of spacecraft and rockets* 56.3, pp. 931–951. DOI: 10.2514/1.A34326 (cit. on p. 32).

Kusche, Jürgen, Roland Schmidt, Svetozar Petrovic, and Roelof Rietbroek (2009). „Decorrelated GRACE time-variable gravity solutions by GFZ, and their validation using a hydrological model“. In: *Journal of geodesy* 83, pp. 903–913. DOI: 10.1007/s00190-009-0308-3 (cit. on p. 34).

Kvas, Andreas (June 2024). *akvas/grates: v0.1.0*. Version v0.1.0. DOI: 10.5281/zenodo.11672421 (cit. on pp. 20, 23, 24).

Landerer, Felix W, Frank M Flechtner, Himanshu Save, et al. (2020). „Extending the global mass change data record: GRACE Follow-On instrument and science data performance“. In: *Geophysical Research Letters* 47.12, e2020GL088306. DOI: 10.1029/2020GL088306 (cit. on pp. 2, 32).

Landerer, Felix W, David N Wiese, Katrin Bentel, Carmen Boening, and Michael M Watkins (2015). „North Atlantic meridional overturning circulation variations from GRACE ocean bottom pressure anomalies“. In: *Geophysical Research Letters* 42.19, pp. 8114–8121. DOI: 10.1002/2015GL065730 (cit. on pp. 3, 17, 20, 53, 55, 58, 61).

McCarthy, Gerard D, Peter J Brown, Charles N Flagg, et al. (2020). „Sustainable observations of the AMOC: methodology and technology“. In: *Reviews of Geophysics* 58.1, e2019RG000654. DOI: 10.1029/2019RG000654 (cit. on p. 1).

McCarthy, Gerard D, David A Smeed, William E Johns, et al. (2015). „Measuring the Atlantic meridional overturning circulation at 26 N“. In: *Progress in Oceanography* 130, pp. 91–111. DOI: 10.1016/j.pocean.2014.10.006 (cit. on pp. 15, 24, 26).

Meyssignac, Benoit, Tim Boyer, Zhongxiang Zhao, et al. (2019). „Measuring global ocean heat content to estimate the Earth energy imbalance“. In: *Frontiers in Marine Science* 6, p. 432. DOI: 10.3389/fmars.2019.00432 (cit. on pp. 12, 13).

Moat, Ben, David Smeed, Darren Rayner, et al. (2023). „Atlantic meridional overturning circulation observed by the RAPID-MOCHA-WBTS (RAPID-Meridional Overturning Circulation and Heatflux Array-Western Boundary Time Series) array at 26N from 2004 to 2022“. Version (v2022.1). In: DOI: 10.5285/04c79ece-3186-349a-e063-6c86abc0158c (cit. on pp. 5, 26–29).

Moat, Ben I, David A Smeed, Eleanor Frajka-Williams, et al. (2020). „Pending recovery in the strength of the meridional overturning circulation at 26 N“. In: *Ocean Science* 16.4, pp. 863–874. DOI: 10.5194/os-16-863-2020 (cit. on pp. 26, 27).

NASA (2024a). *GRACE-FO assembly at Harris Spaceport Systems facility at Vandenberg Air Force Base in California*. URL: https://www.jpl.nasa.gov/images/pia22444-grace-follow-on-assembly (visited on May 19, 2024) (cit. on p. 33).

– (2024b). *Illustration of the twin spacecraft of the GRACE-FO mission*. URL: https://www.jpl.nasa.gov/images/pia22440-grace-follow-on-satellites-artists-concept (visited on May 19, 2024) (cit. on p. 33).

NOAA (2024). *Thermocline*. URL: https://oceanservice.noaa.gov/facts/thermocline.html (visited on May 9, 2024) (cit. on p. 7).

Raymo, Maurenn E (1994). „The initiation of Northern Hemisphere glaciation“. In: *Annual Review of Earth and Planetary Sciences* 22.1, pp. 353–383. DOI: 10.1146/annurev.ea.22.050194.002033 (cit. on p. 10).

Renssen, Hans, Aurélien Mairesse, Hugues Goosse, et al. (2015). „Multiple causes of the Younger Dryas cold period“. In: *Nature Geoscience* 8.12, pp. 946–949. DOI: 10.1038/NGEO2557 (cit. on pp. 15, 16).

Smeed, David A, SA Josey, Claudie Beaulieu, et al. (2018). „The North Atlantic Ocean is in a state of reduced overturning“. In: *Geophysical Research Letters* 45.3, pp. 1527–1533. DOI: 10.1002/2017GL076350 (cit. on pp. 1, 5, 14, 53, 54).

Steiner, Andrea, Barbara Pirscher, Ulrich Foelsche, and Gottfried Kirchengast (2009). *New horizons in occultation research*. Springer. DOI: 10.1007/978-3-642-00321-9 (cit. on p. 2).

Stewart, Robert H. (2006). *Introduction to Physical Oceanography*. Texas A&M University (cit. on pp. 7–9).

Tapley, Byron D, Srinivas Bettadpur, John C Ries, Paul F Thompson, and Michael M Watkins (2004). „GRACE measurements of mass variability in the Earth system“. In: *science* 305.5683, pp. 503–505. DOI: 10.1126/science.1099192 (cit. on pp. 2, 32).

Verein Deutscher Ingenieure, VDI-Gesellschaft Verfahrenstechnik und Chemieingenieurwesen (GVC), K Lucas, and M Luckas (2002). „Berechnungsmethoden für stoffeigenschaften“. In: *VDI-Wärmeatlas: Berechnungsblätter für den Wärmeübergang*, pp. 107–523 (cit. on p. 12).

Von Schuckmann, Karina, Audrey Minière, Flora Gues, et al. (2023). „Heat stored in the Earth system 1960–2020: where does the energy go?“ In: *Earth System Science Data* 15.4, pp. 1675–1709. DOI: 10.5194/essd-15-1675-2023 (cit. on pp. 12, 13).

Westen, René M van, Michael Kliphuis, and Henk A Dijkstra (2024). „Physics-based early warning signal shows that AMOC is on tipping course“. In: *Science advances* 10.6, eadk1189. DOI: 10.1126/sciadv.adk1189 (cit. on pp. 1, 10, 11, 13–16, 54).

Wouters, B, RSW van de Wal, et al. (2018). „Global sea-level budget 1993–present“. In: *Earth System Science Data* 10.3, pp. 1551–1590. DOI: 10.5194/essd-10-1551-2018 (cit. on p. 13).

Zanna, Laure, Samar Khatiwala, Jonathan M Gregory, Jonathan Ison, and Patrick Heimbach (2019). „Global reconstruction of historical ocean heat storage and transport“. In: *Proceedings of the National Academy of Sciences* 116.4, pp. 1126–1131. DOI: 10.1073/pnas.1808838115 (cit. on p. 12).

Imprint

This work was written with LaTeX 2$_\varepsilon$ and the *Clean Thesis* Style was used, developed by Ricardo Langner, available at http://cleanthesis.der-ric.de/. The design *Clean Thesis* was inspired by the written User Guide by Apple Inc.

This template was edited to fulfill the guidelines of the Wegener Center for Climate and Global Change, the Institute of Physics, and the cooperation guidelines, defined by the Karl Franzens University of Graz. This thesis uses the template, released by the *Institute for Geophysics, Astrophysics and Meteorology (IGAM)*[1] on *February 12, 2021*.

[1] https://physik.uni-graz.at/de/igam/

The Atlantic Meridional Overturning Circulation (AMOC) is subject of this work. The basic principles and forcing mechanisms of the AMOC are investigated with the focus on the potential of a new geostrophic approach to estimate meridional transport (MT) in the North Atlantic (NA). This approach is applied to specified oceanic zonal cross-sections and depth layers, using Ocean Bottom Pressure (OBP) data from in-situ, model, and synthetic remote-sensing data. The AMOC accounts for 25 % of the global meridional heat transport, making its overturning system indispensable for maintaining the temperate climate in Europe. Thus, the necessity for a monitoring system of the AMOC that is both spatially and temporally continuous is crucial and well justified. The validity of geostrophic MT estimation using OBP integration along the longitudinal extent of the oceanic cross-section is given through comparisons with in-situ Rapid Climate Change-Meridional Overturning Circulation and Heatflux Array (RAPID) data at 26 °N. Further verification is achieved through Ocean Velocity (OVEL) model data from the Estimating the Circulation and Climate of the Ocean (ECCO) model and synthetic remote sensing data from Gravity Recovery and Climate Experiment/Gravity Recovery and Climate Experiment Follow On (GRACE/GRACE-FO) across the entire NA region. The results imply that MT estimation using solely OBP integration is feasible, given a bathymetry with a gentle slope and sufficient horizontal extent. Strong correlations were particularly noted between the Lower North Atlantic Deep Water (LNADW) and Antarctic Bottom Water (ABW). Additionally, variability signals in one specific layer were found to propagate meridionally. This study underscored the efficacy of geostrophic MT estimation using solely OBP data for observing AMOC variations, thereby assessing latitudinal coherency and long-term variability. Hence, monitoring the variability of the AMOC offers significant potential for tracking changes in the European climate.

Die atlantische meridionale Umwälzzirkulation (AMU) ist Gegenstand dieser Arbeit. Die grundlegenden Prinzipien und Antriebsmechanismen der AMU werden untersucht, wobei der Schwerpunkt auf dem Potenzial eines neuen geostrophischen Ansatzes zur Abschätzung des meridionalen Transports (MT) im Nordatlantik (NA) liegt. Dieser Ansatz wird auf einen bestimmten ozeanischen zonalen Querschnitt und eine Tiefenschicht angewendet, wobei Ozeanbodendruck (OBD)-Daten aus In-situ-, Modell- und synthetischen Fernerkundungsdaten verwendet werden. Die AMU ist für 25 % des globalen meridionalen Wärmetransportes verantwortlich und somit für das gemäßigte Klima in Europa wichtig. Daher ist ein räumlich und zeitlich kontinuierliches Monitoringsystem notwendig und gut begründet. Die Gültigkeit der geostrophischen Transportabschätzung durch OBD-Integration entlang des ozeanischen Querschnitts wird durch Vergleiche mit In-situ Rapid Climate Change-Meridional Overturning Circulation and Heatflux Array (RAPID)-Daten bei 26 °N und Vergleichen mit Estimating the Circulation and Climate of the Ocean (ECCO)-Modell- und Gravity Recovery and Climate Experiment/Gravity Recovery and Climate Experiment Follow On (GRACE/GRACE- FO)-Daten über die gesamte NA-Region belegt. Die Ergebnisse zeigen, dass die Schätzung des meridionalen Transports ausschließlich durch OBD-Integration möglich ist, sofern die Bathymetrie ein gemäßigtes Gefälle und ausreichende horizontale Ausdehnung aufweist. Starke Korrelationen wurden besonders zwischen dem Nordatlantischen Tiefenwasser (NAT) und dem Antarktischen Bodenwasser (ABW) festgestellt. Zudem breiten sich Variabilitätssignale meridional aus. Diese Studie unterstreichte die Wirksamkeit der geostrophischen Transportabschätzung nur durch OBD-Daten zur Beobachtung von AMU-Variationen und zur Bewertung der meridionalen Kohärenz und langfristigen Variabilität. Daher bietet die Überwachung der AMU-Variabilität erhebliches Potenzial für das Monitoring von Veränderungen im europäischen Klima.

SR 104 | 2024 Estimating AMOC's Variability via In-Situ, Synthetic Remote-Sensing and Model Data
Wegener Center Verlag, University of Graz, Austria. ISBN 978-3-9505053-3-7